Multi-Sample and Multi-Group Spatial Colocalization Analysis Using PANORAMIC

Jacob Chang[1], Almudena Espín Pérez[1], Perla Molina[1], Rohit Khurana[1], Weiruo Zhang[1], Lu Tian[1,2], Sylvia Plevritis[1,3,*]

[1]Department of Biomedical Data Science, Stanford University, CA, USA
[2]Department of Statistics, Stanford University, CA, USA
[3]Department of Radiology, Stanford University, CA, USA

*Corresponding author: plevriti@stanford.edu

Abstract

Spatial omics technologies that map cellular organization in individual tissue samples at high resolution require statistical analysis of spatial patterns that accounts for the hierarchical relationship of within- and between-sample variability. Existing spatial statistical methods typically overlook within-sample variability, resulting in unreliable inference and reduced reproducibility when analyzing new groups of samples. We introduce PANORAMIC, a hierarchical framework for efficient estimation and statistical testing of colocalization between pairs of cell types in spatial omics. PANORAMIC integrates spatial bootstrapping to quantify within-sample variability with random-effects meta-analysis to pool information on the colocalization of each cell pair and account for heterogeneity across independent samples within a group. Simulation analyses of images of multiple cell types generated from spatial point process models show that PANORAMIC accurately estimates variance components at the sample and group levels and outperforms naive pooling in key benchmarks. Applied to spatial omics images from colorectal cancer tissue microarrays imaged using a high-multiplexed immunofluorescence platform, PANORAMIC identifies higher colocalization among B- and T-cell subsets in samples with Crohn's-like reactions (CLR) compared with samples exhibiting diffuse inflammatory infiltration (DII). These findings are consistent with tertiary lymphoid structure formation, more favorable prognosis in CLR versus DII, and were missed by existing computational methods. By modeling uncertainty at multiple hierarchical levels and enabling properly powered between-group comparisons, PANORAMIC addresses a gap in spatial omics analysis. PANORAMIC is broadly applicable across single-cell spatial technologies and tissue contexts and is released as an open-source R package, supporting statistical analysis of multi-sample and multi-group spatial omics.

Introduction

Spatially resolved single-cell technologies are transforming the study of tissue architecture by providing quantitative molecular and positional information for thousands of cells within excised tissues [1, 2, 3, 4, 5, 6, 7, 8, 9]. One key analysis in spatial omics is quantifying spatial colocalization between cell types, which serves as a proxy for cellular interaction and shared microenvironment [10, 11]. For example, increased proximity between CD8+ T cells and tumor cells has been associated with improved response to immunotherapy [12], and similar patterns involving B cells, Tregs, and CD4+ T cells are indicative of tertiary lymphoid structures linked to favorable outcomes [13, 14]. These and related findings demonstrate that spatial colocalization patterns encode biologically and clinically meaningful aspects of tissue organization.

Despite the value of colocalization analysis, rigorous statistical comparison of colocalization across samples remains challenging. Each tissue sample can be regarded as a distinct realization of a high-dimensional stochastic spatial process, with thousands of spatially correlated cells nested within samples, and samples nested within patients and clinical groups. This structure results in a hierarchy of variability: within-sample variability arising from local spatial heterogeneity and between-sample variability reflecting biological and technical differences. Standard approaches typically treat sample-level colocalization summaries as error-free point estimates and apply classical hypothesis tests which ignore this nested structure. This can lead to mischaracterization of uncertainty and potential masking or exaggeration of biological differences, especially in small, heterogeneous cohorts.

Several recent methods have begun to address aspects of this problem. For instance, spicyR [15] uses linear mixed-effects models to accommodate multiple images per subject before performing differential colocalization testing, and SpaceANOVA [16] summarizes each sample by a spatial interaction function and applies functional ANOVA to compare colocalization between groups and across cell distances. Simple group-wise tests of spatial statistics, such as colocation quotients, have also been used in applied studies [17, 18, 19]. However, these approaches do not jointly estimate within-sample spatial uncertainty and propagate it through multi-sample pooling. This limitation is particularly consequential for clinically oriented studies, which often focus on small cohorts with substantial biological heterogeneity. The field needs a unified framework that simultaneously respects spatial correlation structure, propagates uncertainty across hierarchical levels, and robustly quantifies between-sample heterogeneity.

We present PANORAMIC (**P**ooled **AN**alysis **O**f Va**R**iance-**A**ware **M**odeling and **I**nference of **C**olocalization), a statistical framework that explicitly models variance at both within- and between-sample levels. PANORAMIC combines spatial bootstrapping, which estimates within-sample uncertainty while preserving spatial correlation, with random-effects meta-analysis to pool estimates across samples and quantify between-sample heterogeneity. This yields a hierarchical approach that provides pooled colocalization estimates across multiple samples alongside model-

based measures of uncertainty.

To evaluate PANORAMIC, we apply it to simulated spatial point-process (SPP) data representing diverse tissue architectures where ground truth is known, as well as multiplexed immunofluorescence images of colorectal cancer tissue microarrays (TMA). Schürch et al. [20] previously analyzed this dataset using CODEX imaging to identify conserved cellular neighborhoods and showed that Crohn's-like reaction (CLR) tumors, when compared to diffuse inflammatory infiltration (DII) tumors, exhibit immune spatial organization associated with favorable prognosis. Building on this dataset, PANORAMIC systematically tests pairwise cell type colocalization patterns while accounting for multiple layers of spatial variance and quantifies the consistency of spatial organization across patients. In addition, network analysis of differential colocalization reveals immune subnetworks in CLR tumors which are consistent with pathologist expectation and the curation of the TMA. Together, these studies demonstrate that PANORAMIC is a practical tool for pooling spatial information across multiple samples under one condition, as well as comparing spatial organization across multiple conditions.

Results

Overview of the PANORAMIC Framework

PANORAMIC enables robust comparison of spatial colocalization across multiple tissue samples using a hierarchical statistical framework that explicitly models within- and between-sample variability. The method consists of three steps: (1) estimating within-sample colocalization with uncertainty quantification for each sample, (2) pooling colocalization estimates across samples to obtain robust group-level summaries, and (3) optionally, testing differential colocalization between groups and performing colocalization network analysis (**Figure 1**).

Step 1: Estimation of within-sample colocalization variability

Each simulated spatial omics sample is represented as a two-dimensional marked point pattern, with cell locations (x, y) and cell type annotations as marks (**Figure 1A**(i)). Samples are stored as a list of SpatialExperiment objects to maintain interoperability with the Bioconductor ecosystem [21]. To describe the analysis, let C index all distinct cell types and define $\mathcal{P} = \{(i, j) \mid i \in C, j \in C\}$. Each $p = (i, j) \in \mathcal{P}$ denotes an ordered pair of cell types, where the first element is the focal cell type and the second is the neighboring cell type in the colocalization statistic described below.

For each pair p and sample k, colocalization is quantified using Ripley's homogeneous cross-L function with translation edge correction (**Supplementary Methods**) [22, 23], over a user-specified range of biologically relevant distances r. The corresponding cross-K statistic $K_{p,k}(r)$ essentially counts neighboring cells of type j within distance r of a focal cell of type i, normalized by cell abundances and tissue area. Since the statistic is directional, the ordering of the cell type pair matters: for example, the cell type pair (endothelial, tumor) refers to the colocalization of

tumor cells as neighboring cells to endothelial cells as focal cells, whereas (tumor, endothelial) refers to the colocalization of endothelial cells as neighboring cells to tumor cells as targets cells.

The cross-L statistic standardizes and centers $K_{p,k}(r)$:

$$L_{p,k}(r) = \sqrt{\frac{K_{p,k}(r)}{\pi}} - r \tag{1}$$

with $L_{p,k}(r) > 0$ indicating greater-than-random colocalization. and $L_{p,k}(r) < 0$ indicating spatial avoidance.

While $L_{p,k}(r)$ provides a useful summary of cell type pair p's colocalization in a tissue sample k, a single point estimate can mask considerable within-sample variability. In some tissues, spatial structure is homogeneous or consistent and $L_{p,k}(r)$ is stable, whereas in others, strong within-sample heterogeneity makes $L_{p,k}(r)$ highly sensitive to the sampled region. To reflect this, PANORAMIC explicitly quantifying within-sample colocalization uncertainty then upweights versus downweights samples with stable versus unstable within-sample colocalization in step 2, described below.

For each p, k, PANORAMIC applies the Loh spatial bootstrap [24, 25] to obtain an empirical sampling distribution of $L_{p,k}(r)$. Per-cell local contributions to the cross-L statistic are computed, resampled with replacement, and recombined to generate bootstrap replicates $L^{(b)}_{p,k}(r), b = 1, \ldots, B$ (**Supplementary Methods**). The bootstrap variance

$$\hat{\sigma}^2_{p,k}(r) = \mathrm{var}\left\{L^{(b)}_{p,k}(r) \mid b = 1, 2, \ldots, B\right\} \approx \frac{1}{B}\sum_{b=1}^{B}\left\{L^{(b)}_{p,k}(r) - L_{p,k}(r)\right\}^2, \tag{2}$$

serves as an estimate of the within-sample sampling variance $\mathrm{var}(L_{p,k}(r))$, thereby avoiding the treatment of the sample-specific colocalization as an error-free point estimate (**Figure 1A**(ii)).

Step 2: Multi-sample pooling with random-effects meta-analysis

To summarize colocalization within a group of samples, PANORAMIC uses a two-level hierarchical random-effects meta-analysis model. At the first level,

$$L_{p,k}(r) \sim \mathcal{N}\left(l_{p,k}(r), \hat{\sigma}^2_{p,k}(r)\right) \tag{3}$$

where $l_{p,k}(r)$ is the unobserved, sample-specific colocalization for cell pair p, and $\hat{\sigma}^2_{p,k}(r)$ is the bootstrap-based variance estimate. At the second level,

$$l_{p,k}(r) \sim \mathcal{N}\left(\mu_p(r), \tau^2_p(r)\right), k = 1, \cdots, K \tag{4}$$

with $\mu_p(r)$ representing the group-level mean colocalization and $\tau_p^2(r)$ the between-sample variance. Marginally,

$$L_{p,k}(r) \sim \mathcal{N}\left(\mu_p(r), \hat{\sigma}_{p,k}^2(r) + \tau_p^2(r)\right), k = 1, 2, \cdots, K. \tag{5}$$

Model parameters are estimated using the Sidik-Jonkman approach [26], which has favorable performance in settings with small to moderate numbers of samples and substantial heterogeneity [27, 28]—features which are common in clinical spatial omics datasets. This procedure yields a pooled mean $\hat{\mu}_p(r)$ with variance

$$\hat{\sigma}_p^2(r) = \left\{ \sum_{k=1}^{K} \frac{1}{\hat{\tau}_p^2(r) + \hat{\sigma}_{p,k}^2(r)} \right\}^{-1}, \tag{6}$$

and an estimate $\hat{\tau}_p^2(r)$ of the between-sample variance. Model fitting is performed independently for each group of samples and each cell type pair $p \in \mathcal{P}$.

These resulting quantities provide pooled, multilevel estimates of colocalization and uncertainty even when no hypothesis testing is performed, and can be summarized by forest plots (**Figure 1B**). For example, one can report that, for pair p in a given group, the pooled mean colocalization is $\hat{\mu}_p(r)$ with variance $\hat{\sigma}_p^2(r)$ and between-sample variance $\hat{\tau}_p^2(r)$, jointly characterizing mean effect, estimates of uncertainty within each sample and across samples of a given group.

Step 3: Hypothesis testing for differential colocalization between groups

To compare the colocalization of pair p between two groups, PANORAMIC uses the Wald test on pooled group-specific estimates. For two non-overlapping groups A and B,

$$Z_p(r) = \frac{\hat{\mu}_p^{(A)}(r) - \hat{\mu}_p^{(B)}(r)}{\sqrt{\hat{\sigma}_p^{(A)}(r)^2 + \hat{\sigma}_p^{(B)}(r)^2}} \tag{7}$$

which is compared to a standard normal reference distribution to obtain two-sided p-values. Multiple testing correction is applied across all pairs $p \in \mathcal{P}$, controlling the false discovery rate (FDR) (**Figure 1C**(i)).

The resulting Z-scores can be visualized in volcano plots and used to construct spatial colocalization networks (**Figure 1C**(ii-iii)), with nodes representing cell types and edge weights derived from $|Z_p(r)|$ between cell type pair p. Algorithms such as Leiden clustering can then reveal subnetworks of cell types that exhibit coordinated differential colocalization between groups (**Supplementary Methods**).

Benchmarking PANORAMIC via Spatial Simulation Studies

To evaluate PANORAMIC under controlled conditions with known ground truth, we performed simulation studies using spatial point process (SPP) models (**Supplementary Methods**). Across diverse spatial architectures, PANORAMIC was assessed on its ability to: (1) recover within-sample

variance from a single tissue realization using spatial bootstrapping, and (2) recover group-level mean colocalization and between-sample heterogeneity using random-effects meta-analysis.

Benchmark study 1: validation of PANORAMIC within-sample variance estimation

We defined three spatial point patterns intended to capture distinct tissue organizations of five cell types (**Figure 2A**): (1) Homogeneous point pattern where the five cell types, two abundant and three rare, are each independently and uniformly distributed across the tissue domain, consistent with complete spatial randomness, (2) Divergent point pattern where two abundant cell types occupy largely non-overlapping regions (mimicking spatial compartmentalization), with the remaining three cell types are rarer and randomly distributed, and (3) Clustered point pattern where one cell type acts as "parent" points and a second cell type as "offspring" within a fixed radius, with the remaining three types distributed randomly. Each scenario includes rare cell types at roughly 5% and 2% frequency. See **Supplementary Simulation Details** for intensity function specifications and parameter values.

Here the goal is to assess whether the "true" within-sample variance obtained from many realizations can be approximated by bootstrap-derived variance from a single realization —mirroring typical spatial omics studies, where tissue availability and the high experimental costs frequently limit the number of sections per sample.

Simulation design. For each spatial point pattern (homogeneous, divergent, clustered), we generated 1000 independent realizations ω_i. For each cell type pair p, we computed $L_{(p,k),i}(r)$ at a fixed distance r, and defined the ground truth within-sample variance as

$$\sigma^2_{p,k}(r) = \mathrm{var}\left\{L_{(p,k),i}(r) \mid i = 1, 2, \ldots, 1000\right\} \tag{8}$$

To mimic a real study, PANORAMIC was then applied to each single realization ω_i, using $B = 100$ bootstrap iterations to estimate $\hat{\sigma}^2_{(p,k),i}(r)$. For each realization, we computed the Pearson correlation between the true $\{\sigma^2_{p,k}(r)\}_p$ and bootstrap estimated $\{\hat{\sigma}^2_{(p,k),i}(r)\}_p$ across all 25 ordered cell type pairs, yielding 1000 correlation coefficients ρ per spatial point pattern.

Results. Spatial bootstrapping showed high correlation with ground truth for homogeneous (median $\rho = 0.71$) and clustered (median $\rho = 0.70$) point patterns for estimating sampling variability (**Figure 2B**). For divergent points patterns, depicting strong compartmentalization of abundant cell types, correlations were more modest (median $\rho = 0.51$), suggesting that local resampling may underrepresent variance when global segregation, rather than local clustering, dominates colocalization. These findings highlight that PANORAMIC's within-sample variance estimates are reliable in many realistic settings but may be conservative in strongly compartmentalized tissues.

Benchmark study 2: validation of PANORAMIC between-sample variance estimation

This benchmark study evaluates PANORAMIC's ability to recover group-level mean colocalization $\mu_p(r)$ and between-sample variance $\tau_p^2(r)$ in the presence of realistic sample-to-sample heterogeneity.

Simulation design. We constructed a hierarchical SPP framework (**Figure 3A**). Starting from a baseline clustered point pattern with parent cell type A and offspring cell type B, we generated K sample-specific variants by perturbing cluster radii, parent intensities, and offspring rates to mimic biological variability across patients (see **Supplementary Simulation Details** for parameter ranges). For each variant (sample) k, 100 independent realization ω_i were simulated and used to define sample-level ground truth:

$$l_{p,k}(r) = \frac{1}{100}\sum_{i=1}^{100} L_{(p,k),i}(r) \tag{9}$$

$$\sigma_{p,k}^2(r) = \frac{1}{100}\sum_{i=1}^{100} \left\{L_{(p,k),i}(r) - l_{p,k}(r)\right\}^2, \tag{10}$$

Group-level ground truth parameters were computed as:

$$\mu_p(r) = \frac{1}{K}\sum_{k=1}^{K} l_{p,k}(r) \tag{11}$$

$$\tau_p^2(r) = \frac{1}{K}\sum_{k=1}^{K} \{l_{p,k}(r) - \mu_p(r)\}^2 \tag{12}$$

To emulate typical experimental designs, PANORAMIC was applied using only a single realization per sample, with spatial bootstrapping to estimate $\hat{\sigma}_{p,k}^2(r)$ and random-effects meta-analysis to estimate $\hat{\mu}_p(r), \hat{\sigma}_p^2(r)$, and $\hat{\tau}_p^2(r)$ (**Figure 3B**). For comparison, we considered naive estimators that ignore within sampling uncertainty:

$$\hat{\mu}_p^{\text{naive}}(r) = \frac{1}{K}\sum_{k=1}^{K} \hat{L}_{p,k}(r) \quad \text{(sample mean)} \tag{13}$$

$$\hat{\tau}_p^{\text{naive}}(r) = \sqrt{\frac{1}{K}\sum_{k=1}^{K} \left\{\hat{L}_{p,k}(r) - \hat{\mu}_p^{\text{naive}}(r)\right\}^2} \quad \text{(sample variance)} \tag{14}$$

where $L_{p,k}(r)$ denotes the single observed colocalization per sample. We evaluated performance over $K \in [2, 100]$ by computing RMSE between estimated and ground truth values for $\mu_p(r)$ and $\tau_p^2(r)$, repeating the procedure multiple times to obtain variability bands (**Figure 3C-D**).

Results. PANORAMIC achieved lower root mean squared error (RMSE) than naive estimators for both $\mu_p(r)$ and $\tau_p^2(r)$ across most sample sizes and cell type pairs. As K increased, both approaches converged toward the true mean; for very large K, naive estimation of $\mu_p(r)$ was

competitive, whereas PANORAMIC retained a clear advantage for estimating $\tau_p^2(r)$. Naive variance estimates systematically inflated $\tau_p^2(r)$, reflecting conflation of within-sample noise with true between-sample heterogeneity, whereas PANORAMIC's hierarchical model more cleanly separated these sources of variation. This improved estimation of heterogeneity is particularly relevant when interpreting spatial variability across patients or conditions.

Applying PANORAMIC to Reveal Colorectal Cancer Immune Spatial Architecture

To assess PANORAMIC in a clinically relevant setting, we analyzed a CODEX multiplex imaging dataset from colorectal cancer tissue microarrays comprising 35 tumor cores from the invasive front, classified as Crohn's-like reaction (CLR, $n = 17$) or diffuse inflammatory infiltration (DII, $n = 18$), published by by Schürch et al. [20]. CLR tumors are known to exhibit organized peritumoral lymphoid aggregates resembling tertiary lymphoid structures, which have been associated with favorable prognosis, whereas DII tumors show more dispersed immune infiltration [20, 29, 30].

Using PANORAMIC, we systematically compared pairwise colocalization between cell types across the CLR and DII groups, quantified between-sample heterogeneity within each group, and used differential colocalization scores to construct higher-order colocalization subnetworks.

PANORAMIC identifies increased B- and T-cell colocalization in CLR

The cell types annotated by Schürch et al. yielded 169 ordered cell type pairs (**Supplementary Figure E.1**). When focused on a colocalization at $r = 75\mu$m, PANORAMIC identified nine pairs with significantly higher colocalization in CLR than DII after FDR correction, predominantly involving B cells, CD4+CD45RO+ T cells, CD8+ T cells, and Tregs (**Figure 4A**). No pairs showed significantly higher colocalization in DII at $r = 75\mu$m. **Figure 4B** provides representative cores with colocalization values nearest to group means, further contextualizing these summaries by illustrating dense, organized immune clusters in CLR and more dispersed immune cells in DII.

The enriched pairs identified in CLR are consistent with the cellular components of tertiary lymphoid structures and align with previous qualitative descriptions of organized immune neighborhoods in CLR [29, 30, 20]. Multi-length analyses across radii (r) from 50-150 μm produced similar quantitative patterns, with broader radii capturing additional significant immune pairs (**Supplementary Figure E.2**).

For comparison, we applied spicyR [15], a linear mixed-effects approach for spatial colocalization. Under analogous settings (same pairs, distance scale r, and FDR threshold), this method did not detect any significant differences between CLR and DII (**Supplementary Table C.1**), whereas PANORAMIC identified multiple immune associations consistent with TLS biology. This contrast underscores the potential impact of explicitly modeling within-sample uncertainty and between-sample heterogeneity when performing group comparisons.

Forest plots illustrate variance decomposition and heterogeneity

To illustrate PANORAMIC's variance decomposition, we examined forest plots for the two most significant cell type pairs: (B cell, B cell) and (CD4+CD45RO+ T cell, Treg) (**Figure 5**). Each plot displays sample-level cross-L estimates with bootstrap-based confidence intervals alongside pooled random-effects estimates for CLR and DII.

For the homotypic cell pair colocalization (B cell, B cell), CLR cores cluster around a higher pooled mean (53.20, SE: 5.00) with all but one sample exceeding the complete spatial randomness reference, whereas DII cores cluster lower and closer to baseline (22.52, SE: 5.09). For CD4+CD45RO+ T cell-Treg colocalization, CLR also shows higher pooled means compared to DII (11.69, SE: 1.12 for CLR versus 5.46, SE: 1.05 for DII). The forest plots highlight how PANORAMIC simultaneously exposes within-sample uncertainty and between-sample variability, rather than collapsing information into a single estimate and p-value. The forest plots also facilitate visual inspection for outlying cores with atypical colocalization patterns.

PANORAMIC network analysis reveals coordinated immune subnetworks in CLR

Pairwise colocalization analyses capture specific relationships but do not directly reveal higher-order coordination among multiple cell types. To explore such organization, we propose a differential colocalization network using PANORAMIC Z-scores as edge weights (**Figure 6A**). Because cross-L is asymmetric, the test yields two directed Z-scores per unordered pair; these were combined into a single undirected weight following a procedure detailed in **Supplementary Methods**. Focusing on CLR-enriched associations and applying Leiden clustering identified subnetworks of cell types with coordinated differential colocalization.

One prominent subnetwork in CLR comprised B cells, CD4+CD45RO+ T cells, CD8+ T cells, and Tregs, consistent with a TLS-like immune hub. To test whether this pattern reflects a genuine spatial higher-order colocalization network rather than network construction artifacts, we computed, for each sample, the average minimum distance from each subnetwork cell to its nearest neighbor of each other subnetwork cell type (including homotypic neighbors). This summary captures the typical spacing among cells participating in the putative immune hub.

CLR samples showed significantly smaller average minimum distances than DII samples, indicating tighter spatial organization of the subnetwork (one-sided t-test, $p = 0.03$) (**Figure 6B**). Representative cores from each phenotype with distances nearest to group means visually confirm this pattern: in CLR, the four immune types co-aggregate into compact clusters, whereas in DII they are more dispersed (**Figure 6C**(i-ii)). Together, these results support the presence of a coordinated immune subnetwork in CLR that is consistent with, and extend, prior descriptions of cellular neighborhoods.

Discussion

Spatial omics studies comparing tissue spatial organization across patient groups and conditions typically rely on statistical methods that ignore within-sample spatial uncertainty, leading to inadequate quantification of within-group sample heterogeneity and unreliable inference in group comparisons. PANORAMIC introduces a hierarchical framework for multi-sample and multi-group spatial colocalization analysis that explicitly models both within-sample spatial uncertainty and between-sample heterogeneity, and thereby enables more robust statistical inference.

PANORAMIC's core innovation is a multilevel variance modeling framework tailored to spatial omics data. This framework is applied to the colocalization assessment, where the observed colocalization statistic $L_{p,k}(r)$ is treated as an estimator of an underlying colocalization summary $l_{p,k}(r)$ with sampling variance $\sigma^2_{p,k}(r)$ determined by the tissue's spatial configuration. Spatial bootstrapping resamples local contributions while preserving spatial dependence, providing within-sample uncertainty estimates that are then propagated through a hierarchical random-effects meta-analysis.

The hierarchical framework in PANORAMIC yields two main benefits. First, pooled estimates $\hat{\mu}_p(r)$ have improved efficiency because they account for heterogeneous sampling noise across samples. Second, the framework provides heterogeneity estimates $\hat{\tau}^2_p(r)$ that quantify variation in spatial organization across groups of patients or conditions, offering a biologically interpretable summary that is often missing from simpler approaches. Forest plots naturally summarize both sampling uncertainty and between-sample variability, facilitating transparent interpretation of spatial effects across cohorts.

A spatial point process simulation model was introduced to evaluate performance of PANORAMIC under controlled spatial architectures that mimic realistic spatial omics studies. By generating synthetic tissues with known within- and between-sample variance components and then attempting to recover these from single realizations, the simulations demonstrate that PANORAMIC can accurately estimate both levels of variance and outperform naive pooling strategies.

In the colorectal cancer application, PANORAMIC identifies colocalization patterns which distinguish Crohn's-like reaction (CLR) from diffuse inflammatory infiltration (DII). In CLR samples, PANORAMIC detects higher colocalization between B cells and T-cell subsets consistent with tertiary lymphoid structure (TLS) organization, whereas DII samples show comparatively weaker or more spatially diffuse immune-immune colocalization. These group-level differences are not detected by methods which ignore within-sample sampling variance. Moreover, PANORAMIC reports its results with an explicit distinction between within-sample and between-sample variance, which is critical for demonstrating that reported CLR–DII differences reflect consistent shifts across samples and are not driven by a small number of noisy or atypical samples. Beyond pairwise effects, we showed that constructing differential colocalization networks from pooled estimates and Z-cores from hypothesis testing highlights immune groups that may reflect higher-order organization

characteristic of CLR versus DII samples.

The PANORAMIC framework is flexible. PANORAMIC requires only that the chosen spatial colocalization statistic admit an estimate of within-sample variance, allowing users to alternate among cross-L, cross-K, pair correlation functions, colocation quotient, or other user-defined measures. Likewise, the methodology applies broadly across spatial omics platforms, including multiplexed imaging and spatial transcriptomics, and is agnostic to specific tissue types or disease contexts.

In summary, PANORAMIC provides a practical way to make multi-sample spatial colocalization results interpretable at the cohort level by separating within-sample sampling uncertainty from between-sample variability. The resulting pooled effects and heterogeneity estimates can be directly reported (e.g., via forest plots and higher-order subnetworks) to support robust and transparent comparison across groups. Future work can extend PANORAMIC's uncertainty-propagation principle to additional spatial summaries and to study designs involving more groups or covariates, without altering the underlying workflow.

Data Availability

The colorectal cancer TMA data was previously published by Schurch et al. [20].

Code Availability

The source code for the PANORAMIC framework is released as an R package: https://github.com/plevritis-lab/panoramic (DOI: 10.5281/zenodo.17783979). All scripts used to conduct the analyses and generate the figures presented in this manuscript are provided at: https://github.com/chang-jacob/panoramic_paper.

References

1. Giesen C, Wang HAO, Schapiro D, Zivanovic N, Jacobs A, Hattendorf B, Schüffler PJ, Grolimund D, Buhmann JM, Brandt S, Varga Z, Wild PJ, Günther D, and Bodenmiller B. Highly multiplexed imaging of tumor tissues with subcellular resolution by mass cytometry. Nature Methods 2014 Apr; 11:417–22. DOI: 10.1038/nmeth.2869
2. Chen KH, Boettiger AN, Moffitt JR, Wang S, and Zhuang X. Spatially resolved, highly multiplexed RNA profiling in single cells. Science 2015 Apr; 348. DOI: 10.1126/science.aaa6090
3. Wang X, Allen WE, Wright MA, Sylwestrak EL, Samusik N, Vesuna S, Evans K, Liu C, Ramakrishnan C, Liu J, Nolan GP, Bava FA, and Deisseroth K. Three-dimensional intact-tissue sequencing of single-cell transcriptional states. Science 2018; 361. DOI: 10.1126/science.aat5691

4. Codeluppi S, Borm LE, Zeisel A, La Manno G, Van Lunteren JA, Svensson CI, and Linnarsson S. Spatial organization of the somatosensory cortex revealed by osmFISH. Nature Methods 2018 Nov; 15:932–5. DOI: 10.1038/s41592-018-0175-z
5. Rodriques SG, Stickels RR, Goeva A, Martin CA, Murray E, Vanderburg CR, Welch J, Chen LM, Chen F, and Macosko EZ. Slide-seq: A scalable technology for measuring genome-wide expression at high spatial resolution. Science 2019 Mar
6. Goltsev Y, Samusik N, Kennedy-Darling J, Bhate S, Hale M, Vazquez G, Black S, and Nolan GP. Deep Profiling of Mouse Splenic Architecture with CODEX Multiplexed Imaging. Cell 2018 Aug; 174:968–981.e15. DOI: 10.1016/j.cell.2018.07.010
7. Keren L, Bosse M, Thompson S, Risom T, Vijayaragavan K, McCaffrey E, Marquez D, Angoshtari R, Greenwald NF, Fienberg H, Wang J, Kambham N, Kirkwood D, Nolan G, Montine TJ, Galli SJ, West R, Bendall SC, and Angelo M. MIBI-TOF: A multiplexed imaging platform relates cellular phenotypes and tissue structure. Science Advances 2019 Oct; 5:eaax5851. DOI: 10.1126/sciadv.aax5851
8. He S, Bhatt R, Brown C, Brown EA, Buhr DL, Chantranuvatana K, Danaher P, Dunaway D, Garrison RG, Geiss G, Gregory MT, Hoang ML, Khafizov R, Killingbeck EE, Kim D, Kim TK, Kim Y, Klock A, Korukonda M, Kutchma A, Lewis ZR, Liang Y, Nelson JS, Ong GT, Perillo EP, Phan JC, Phan-Everson T, Piazza E, Rane T, Reitz Z, Rhodes M, Rosenbloom A, Ross D, Sato H, Wardhani AW, Williams-Wietzikoski CA, Wu L, and Beechem JM. High-plex Multiomic Analysis in FFPE at Subcellular Level by Spatial Molecular Imaging. 2021 Nov. DOI: 10.1101/2021.11.03.467020
9. Janesick A, Shelansky R, Gottscho AD, Wagner F, Williams SR, Rouault M, Beliakoff G, Morrison CA, Oliveira MF, Sicherman JT, Kohlway A, Abousoud J, Drennon TY, Mohabbat SH, Teams 1D, and Taylor SEB. High resolution mapping of the tumor microenvironment using integrated single-cell, spatial and in situ analysis. Nature Communications 2023 Dec; 14:8353. DOI: 10.1038/s41467-023-43458-x
10. Schapiro D, Jackson HW, Raghuraman S, Fischer JR, Zanotelli VRT, Schulz D, Giesen C, Catena R, Varga Z, and Bodenmiller B. histoCAT: analysis of cell phenotypes and interactions in multiplex image cytometry data. Nature Methods 2017; 14:873–6. DOI: 10.1038/nmeth.4391
11. Jackson HW, Fischer JR, Zanotelli VRT, Ali HR, Mechera R, Soysal SD, Moch H, Muenst S, Varga Z, Weber WP, and Bodenmiller B. The single-cell pathology landscape of breast cancer. Nature 2020 Feb; 578:615–20. DOI: 10.1038/s41586-019-1876-x
12. Giraldo NA, Sanchez-Salas R, Peske JD, Vano Y, Becht E, Petitprez F, Validire P, Ingels A, Cathelineau X, Fridman WH, and Sautès-Fridman C. The clinical role of the TME in solid cancer. British Journal of Cancer 2019 Jan; 120:45–53. DOI: 10.1038/s41416-018-0327-z
13. Sautès-Fridman C, Petitprez F, Calderaro J, and Fridman WH. Tertiary lymphoid structures in the era of cancer immunotherapy. Nature Reviews Cancer 2019; 19:307–25. DOI: 10.1038/s41568-019-0144-6
14. Helmink BA, Reddy SM, Gao J, Zhang S, Basar R, Thakur R, Yizhak K, Sade-Feldman M, Blando J, Han G, Gopalakrishnan V, Xi Y, Zhao H, Amaria RN, Tawbi HA, Cogdill AP, Liu

W, LeBleu VS, Kugeratski FG, Patel S, Davies MA, Hwu P, Lee JE, Gershenwald JE, Lucci A, Arora R, Woodman S, Keung EZ, Gaudreau PO, Reuben A, Spencer CN, Burton EM, Haydu LE, Lazar AJ, Zapassodi R, Hudgens CW, Ledesma DA, Ong S, Bailey M, Warren S, Rao D, Krijgsman O, Rozeman EA, Peeper D, Blank CU, Schumacher TN, Butterfield LH, Zelazowska MA, McBride KM, Kalluri R, Allison J, Petitprez F, Fridman WH, Sautès-Fridman C, Hacohen N, Rezvani K, Sharma P, Tetzlaff MT, Wang L, and Wargo JA. B cells and tertiary lymphoid structures promote immunotherapy response. Nature 2020 Jan; 577:549–55. DOI: 10.1038/s41586-019-1922-8

15. Canete NP, Iyengar SS, Ormerod JT, Baharlou H, Harman AN, and Patrick E. spicyR: spatial analysis ofin situcytometry data in R. Bioinformatics 2022 May; 38. Ed. by Kelso J:3099–105. DOI: 10.1093/bioinformatics/btac268
16. Seal S, Neelon B, Angel PM, O'Quinn EC, Hill E, Vu T, Ghosh D, Mehta AS, Wallace K, and Alekseyenko AV. SpaceANOVA: Spatial Co-occurrence Analysis of Cell Types in Multiplex Imaging Data Using Point Process and Functional ANOVA. Journal of Proteome Research 2024 Apr; 23:1131–43. DOI: 10.1021/acs.jproteome.3c00462
17. Leslie TF and Kronenfeld BJ. The Colocation Quotient: A New Measure of Spatial Association Between Categorical Subsets of Points. Geographical Analysis 2011; 43:306–26. DOI: 10.1111/j.1538-4632.2011.00821.x
18. Zhang W, Li I, Reticker-Flynn NE, Good Z, Chang S, Samusik N, Saumyaa S, Li Y, Zhou X, Liang R, Kong CS, Le QT, Gentles AJ, Sunwoo JB, Nolan GP, Engleman EG, and Plevritis SK. Identification of cell types in multiplexed in situ images by combining protein expression and spatial information using CELESTA. Nature Methods 2022 Jun; 19:759–69. DOI: 10.1038/s41592-022-01498-z
19. Yeh CY, Aguirre K, Laveroni O, Kim S, Wang A, Liang B, Zhang X, Han LM, Valbuena R, Bassik MC, Kim YM, Plevritis SK, Snyder MP, Howitt BE, and Jerby L. Mapping spatial organization and genetic cell-state regulators to target immune evasion in ovarian cancer. Nature Immunology 2024 Oct; 25:1943–58. DOI: 10.1038/s41590-024-01943-5
20. Schürch CM, Bhate SS, Barlow GL, Phillips DJ, Noti L, Zlobec I, Chu P, Black S, Demeter J, McIlwain DR, Kinoshita S, Samusik N, Goltsev Y, and Nolan GP. Coordinated Cellular Neighborhoods Orchestrate Antitumoral Immunity at the Colorectal Cancer Invasive Front. Cell 2020 Sep; 182:1341–1359.e19. DOI: 10.1016/j.cell.2020.07.005
21. Righelli D, Weber LM, Crowell HL, Pardo B, Collado-Torres L, Ghazanfar S, Lun ATL, Hicks SC, and Risso D. SpatialExperiment: infrastructure for spatially-resolved transcriptomics data in R using Bioconductor. Bioinformatics 2022 May; 38. Ed. by Boeva V:3128–31. DOI: 10.1093/bioinformatics/btac299
22. Ripley BD. The Second-Order Analysis of Stationary Point Processes. Journal of Applied Probability 1976 Jun
23. Baddeley A, Rubak E, and Turner R. Spatial Point Patterns: Methodology and Applications with R. Boca Raton, FL: Chapman and Hall/CRC Press, 2015

24. Loh JM. A Valid and Fast Spatial Bootstrap for Correlation Functions. The Astrophysical Journal 2008 Jul; 681:726–34. DOI: 10.1086/588631
25. Loh JM. Bootstrapping an inhomogeneous point process. Journal of Statistical Planning and Inference 2010 Mar; 140:734–49. DOI: 10.1016/j.jspi.2009.09.003
26. Sidik K and Jonkman JN. Simple Heterogeneity Variance Estimation for Meta-Analysis. Journal of the Royal Statistical Society Series C: Applied Statistics 2005 Apr; 54:367–84. DOI: 10.1111/j.1467-9876.2005.00489.x
27. Röver C, Knapp G, and Friede T. Hartung-Knapp-Sidik-Jonkman approach and its modification for random-effects meta-analysis with few studies. BMC Medical Research Methodology 2015 Dec; 15:99. DOI: 10.1186/s12874-015-0091-1
28. IntHout J, Ioannidis JP, and Borm GF. The Hartung-Knapp-Sidik-Jonkman method for random effects meta-analysis is straightforward and considerably outperforms the standard DerSimonian-Laird method. BMC Medical Research Methodology 2014 Dec; 14:25. DOI: 10.1186/1471-2288-14-25
29. Haruki K, Kosumi K, Li P, Arima K, Väyrynen JP, Lau MC, Twombly TS, Hamada T, Glickman JN, Fujiyoshi K, Chen Y, Du C, Guo C, Väyrynen SA, Dias Costa A, Song M, Chan AT, Meyerhardt JA, Nishihara R, Fuchs CS, Liu L, Zhang X, Wu K, Giannakis M, Nowak JA, and Ogino S. An integrated analysis of lymphocytic reaction, tumour molecular characteristics and patient survival in colorectal cancer. British Journal of Cancer 2020 Apr; 122:1367–77. DOI: 10.1038/s41416-020-0780-3
30. Maoz A, Dennis M, and Greenson JK. The Crohn's-Like Lymphoid Reaction to Colorectal Cancer-Tertiary Lymphoid Structures With Immunologic and Potentially Therapeutic Relevance in Colorectal Cancer. Frontiers in Immunology 2019 Aug; 10:1884. DOI: 10.3389/fimmu.2019.01884

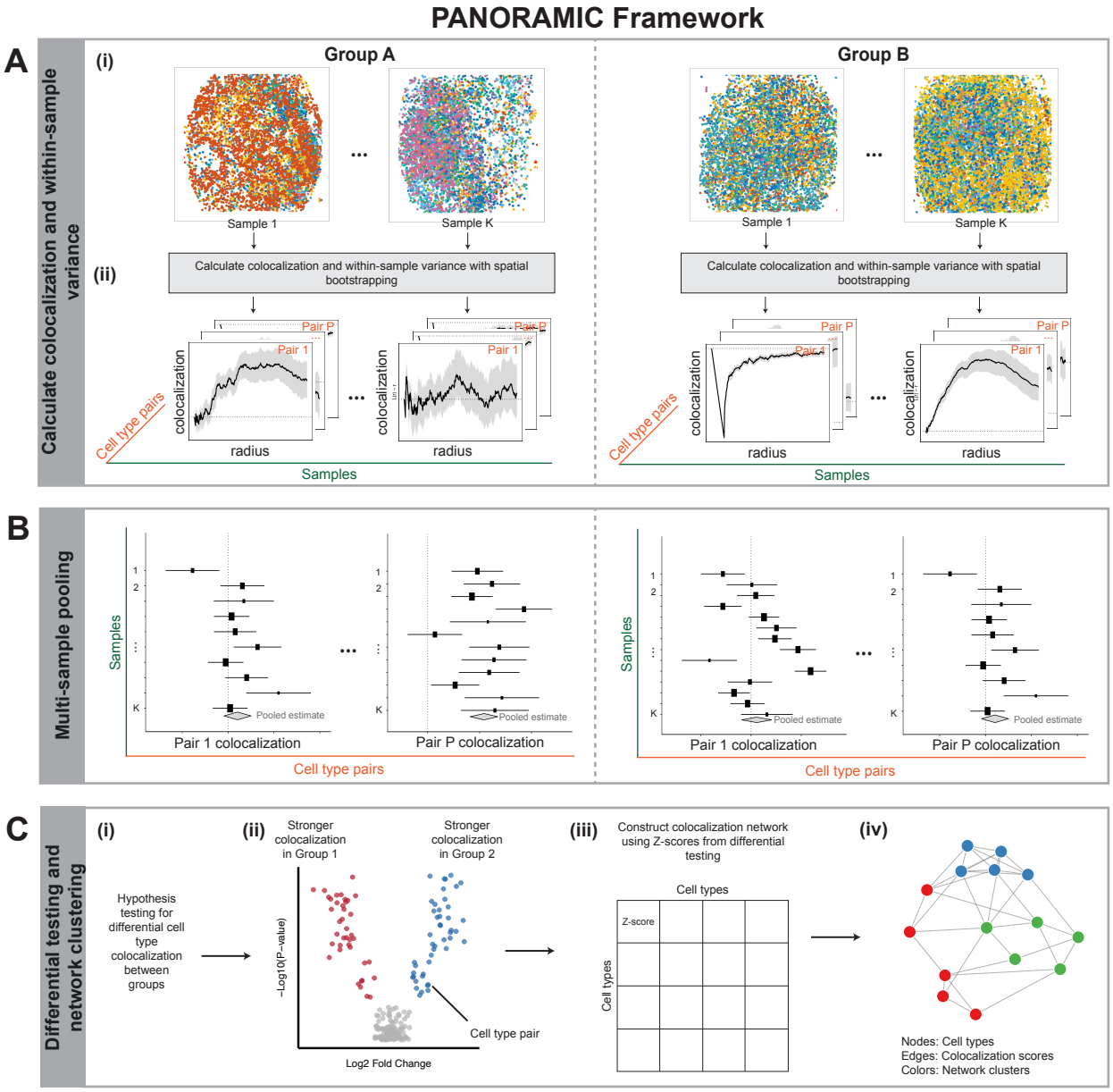

Figure 1. Overview of the PANORAMIC framework. (A) Calculation of colocalization and within-sample variance for each sample. (i) Spatial omics input data (cell type annotations and coordinates) formatted as a list of SpatialExperiment objects. (ii) For each sample k and cell type pair p, compute colocalization and estimate within-sample variance using spatial bootstrapping (depicted by gray-band). **(B)** Multi-sample pooling. For each cell type pair p, pool samples within a group via random-effects meta-analysis. Forest plots show individual sample estimates with within-sample variance and pooled group means (gray diamonds). **(C)** Differential testing and network analysis. (i) Pooled means and standard errors are used to perform hypothesis testing for colocalization differences between groups A and B. (ii) Statistically significant cell type pairs visualized via volcano plot. Each point represents a cell type pair p. (iii) Colocalization matrix is constructed, populated by Z-scores between cell type pairs from the differential testing step. (iv) Network clustering is performed to identify higher-order colocalization subnetworks.

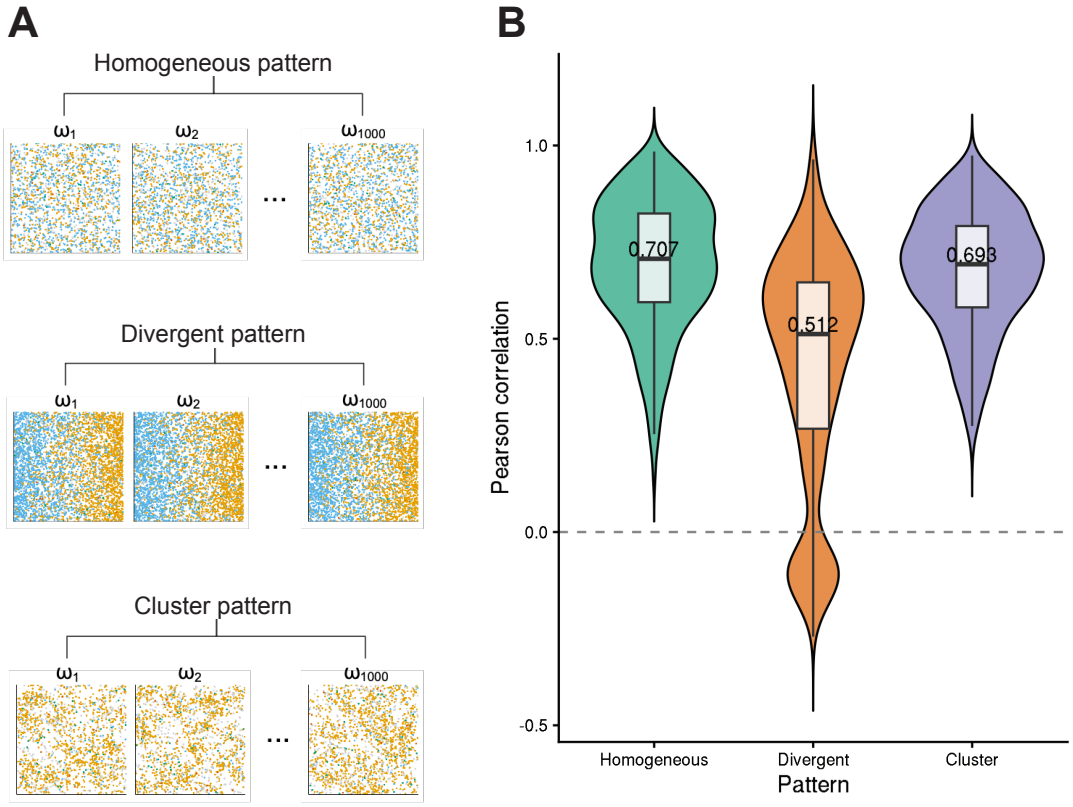

Figure 2. Validation of within-sample variance estimation via spatial bootstrapping. (A) Three spatial point process configurations were used for simulation: (i) homogeneous point pattern (complete spatial randomness), (ii) divergent point pattern (spatial segregation with two cell types localized to opposite regions), and (iii) clustered point pattern (offspring occurring around parent cells). Cell types A, B, C are abundant; Rare 1 and Rare 2 represent low-frequency populations. **(B)** For each configuration, 1000 independent realizations were generated to establish ground truth within-sample variance. Spatial bootstrapping (100 iterations) was applied to each individual realization, and Pearson correlation between bootstrap-derived variance and ground truth was computed across all cell type pairs (25 ordered pairs). Violin plots show distribution of correlations across 1000 realizations, with median values labeled. Spatial bootstrapping shows high concordance for homogeneous (median r = 0.71) and clustered (r = 0.70) point pattersn, indicating accurate variance recovery for these spatial configurations. Concordance is moderate for the divergent point pattern (r = 0.51).

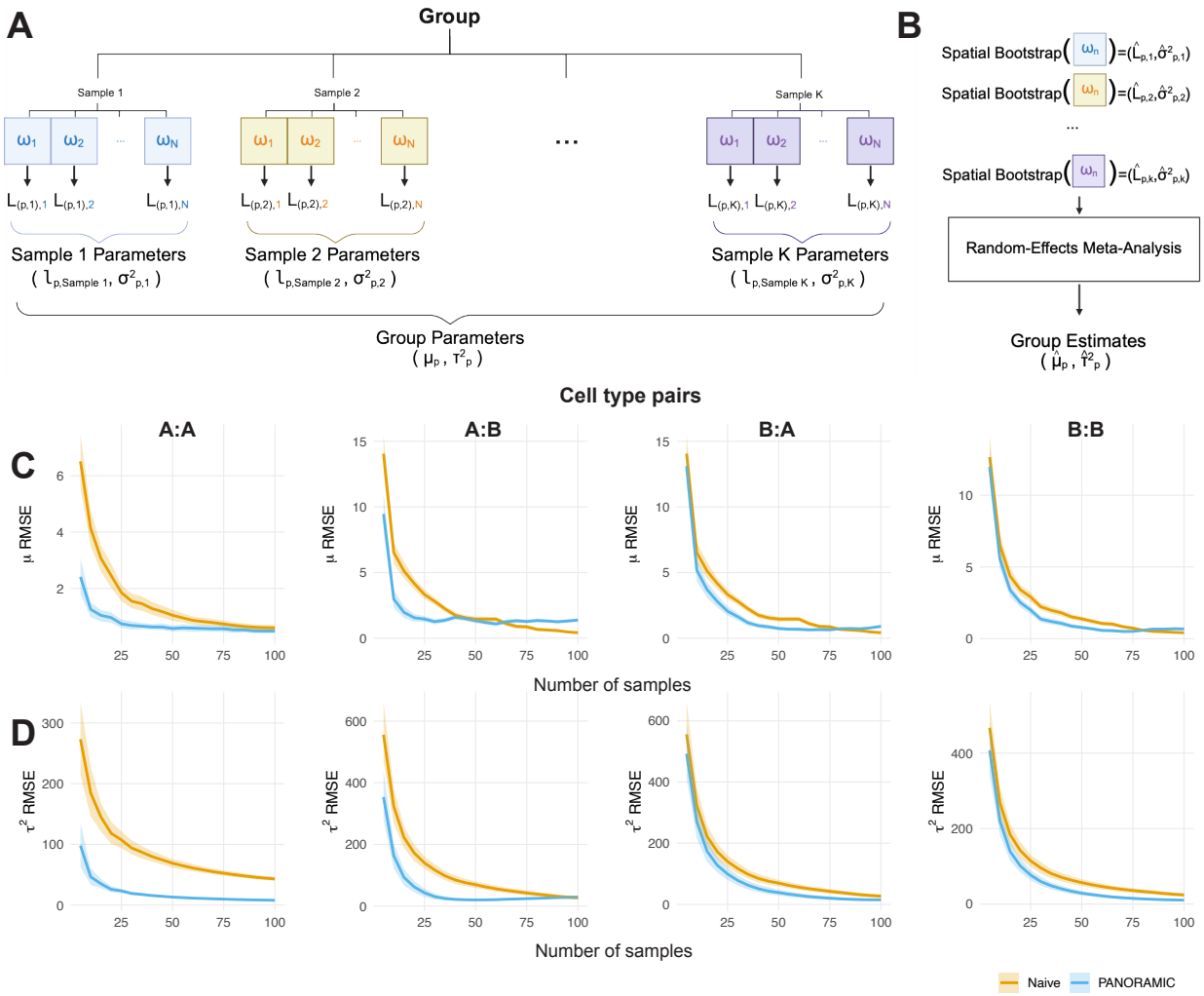

Figure 3. Validation of between-sample variance estimation using PANORAMIC. (A) Hierarchical simulation framework: a baseline SPP model representing an underlying spatial pattern with additional variance added to create K sample-specific variant models representing distinct samples with between-sample heterogeneity. Multiple realizations from each sample variant establish ground truth parameters: sample-specific means $l_{p,k}$, group-level mean μ_p, and between-sample variance τ_p^2. **(B)** PANORAMIC is applied using only one realization per sample (realistic scenario), with spatial bootstrapping estimating within-sample variance $\hat{\sigma}_{p,k}^2$ and random-effects meta-analysis pooling to estimate $\hat{\mu}_p$ and $\hat{\tau}_p^2$. **(C)** Root mean squared error (RMSE) for group mean estimate $\hat{\mu}_p$ versus ground truth across sample sizes $K = 2$ to 100, comparing PANORAMIC (blue) to naive sample mean (orange) for four cell type pairs. **(D)** RMSE for between-sample variance estimate $\hat{\tau}_p^2$ versus ground truth. PANORAMIC accurately partitions within- vs. between-sample variance, whereas naive sample variance conflates these sources, leading to systematic overestimation (orange curves consistently above blue). PANORAMIC's advantage persists across all sample sizes.

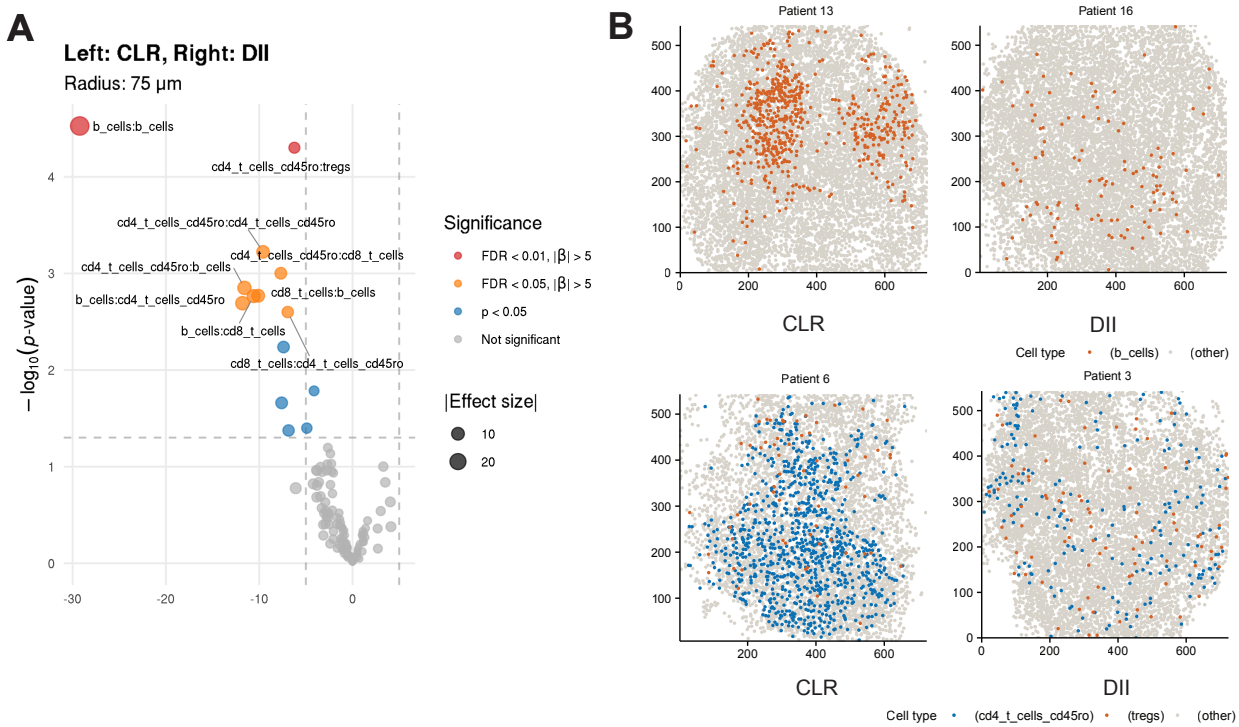

Figure 4. PANORAMIC identifies significantly colocalizaed cell type pairs i colorectal cancer. (A) Volcano plot showing differential colocalization between colorectal cancer phenotypes CLR and DII at 75 μm. Each point represents a cell-type pair, with the effect size on the x-axis defined as the difference in pooled cross-L means (CLR-DII) and y-axis as the p-values from PANORAMIC's Wald test. Points are coloroed by significance and effect size. Nine cell type pairs show significantly elevated colocalization in CLR after multiple testing correction. **(B)** Representative CLR and DII tissue cores for B cell-B cell (top) and CD4+CD45RO+ T cell-Treg (bottom) colocalization, chosen with colocalization values nearest to the respective group means. Colored points highlight the relevant cell type populations; gray points denote other cell types.

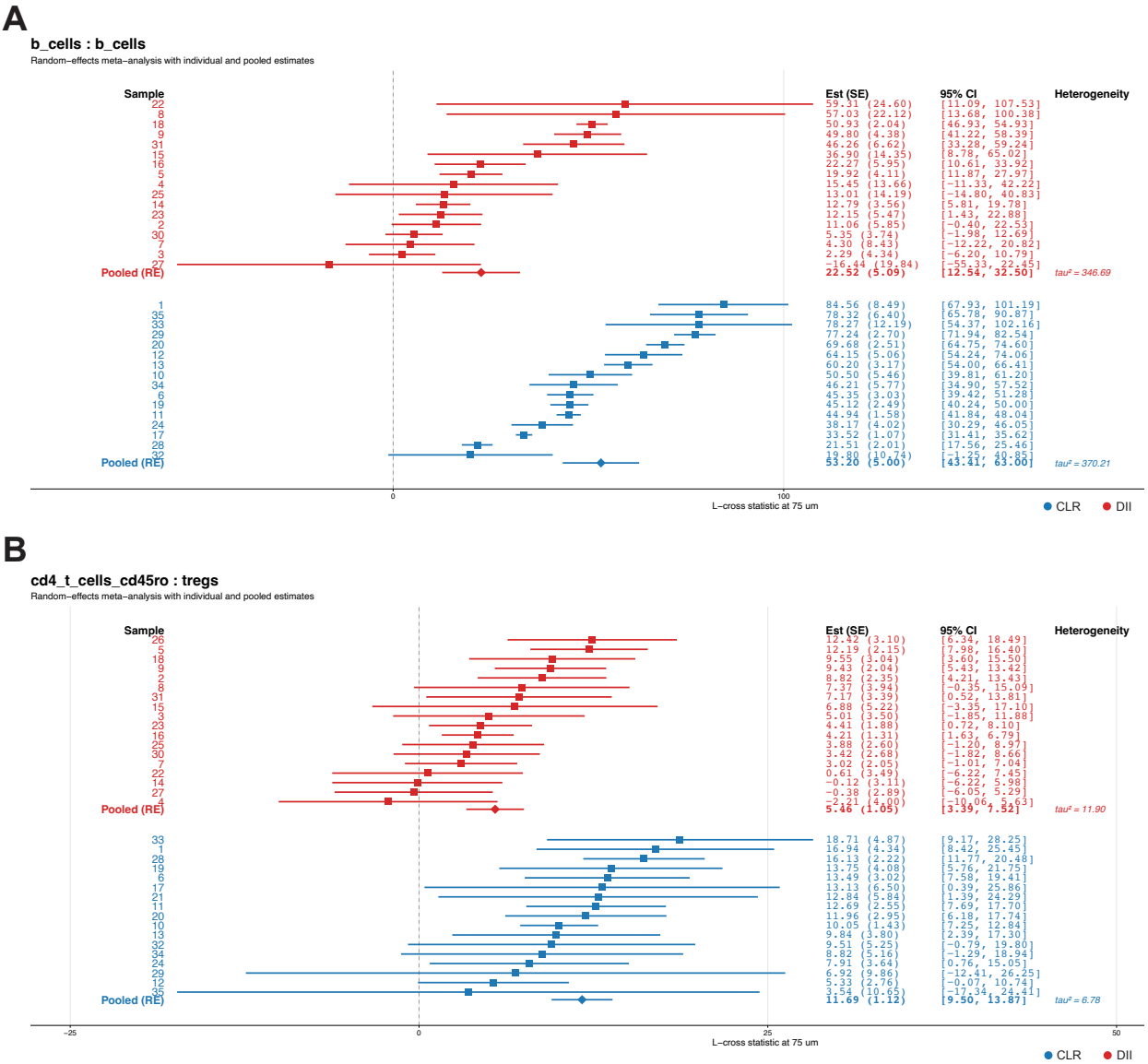

Figure 5. Forest plots of random-effects meta-analysis of spatial colocalization. Representative cell-type pairs from PANORAMIC are visualized, showing individual-sample cross-L estimates (squares) with 95% confidence intervals and pooled random-effects colocalization estimates (diamonds), at 75μm, for each group. Each row corresponds to a tissue core; color encodes group membership (CLR (red) vs DII (blue)), and the right-hand columns report the estimated colocalization, standard error, confidence intervals, and between-sample heterogeneity (τ^2) within each group. Pooled (RE) refers to the pooled colocalization estimate from the random-effects (RE) meta-analysis. **(A)** Forest plot for B cell to B cell homotypic colocalization. **(B)** Forest plot for CD4+ T cells and regulatory T cells heterotypic colocalization.

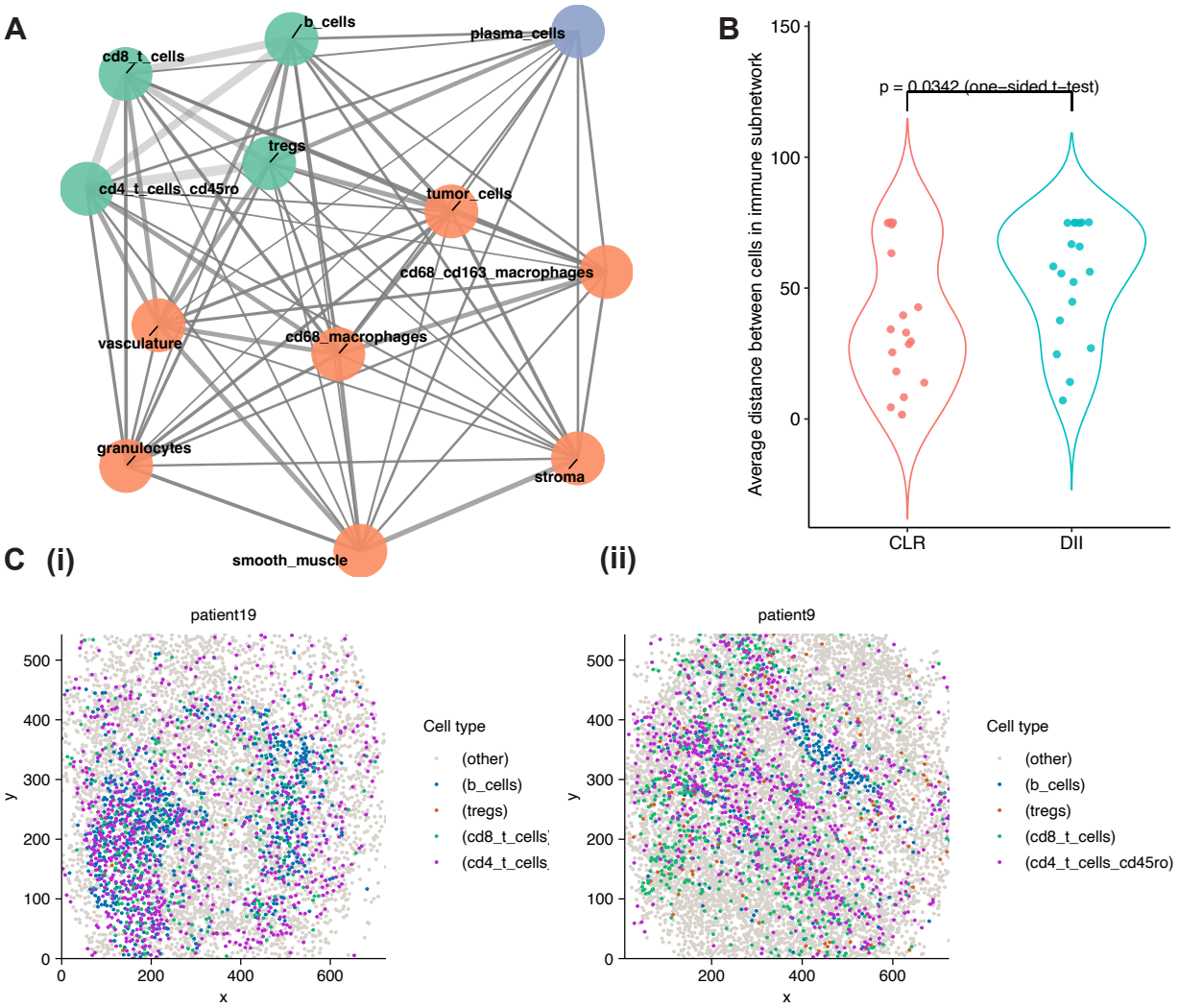

Figure 6. Network analysis reveals coordinated immune subnetworks in CLR. (A) Differential colocalization network constructed from PANORAMIC Z-scores for CLR-enriched associations. Edges are weighted by the magnitude of Wald Z-scores from differential testing between CLR and DII groups, and Leiden clustering identifies three subnetworks (node colors). **(B)** To validate spatial compactness of the green immune subnetwork, we computed, for each tissue core, the average minimum distance from each immune cell to its nearest neighbors of each other subnetwork cell type. CLR samples show significantly shorter distances than DII ($p = 0.03$, one-sided t-test), indicating tighter spatial organization. **(C)** Representative CLR and DII cores illustrate compact immune clustering in CLR versus dispersed infiltration in DII.

Appendices

A Supplementary Methods

A.1 Spatial Colocalization Statistics

A.1.1 Local and Global Cross-K and Cross-L Functions

PANORAMIC uses local versions of the cross-K statistics as building blocks, where statistics are computed at the level of individual cells rather than globally. For cell i' of type i, the local cross-K function with respect to type j is:

$$K_{(i,j)}(i' \mid r) = \frac{|W|}{N_j} \sum_{j'=1}^{N_j} \mathbf{1}[d(i', j') \leq r] \cdot e(i', j') \tag{15}$$

where $|W|$ is the total issue area, N_j is the count of type-j cells, $\mathbf{1}[\cdot]$ is an indicator function, $d(i', j')$ is the distance between type-i cell i' and type-j cell j', and $e(i', j')$ is an edge correction factor.

The global K-statistic is the average of local statistics:

$$K_{(i,j)}(r) = \frac{1}{N_i} \sum_{i'=1}^{N_i} K_{(i,j)}(i' \mid r) = \frac{|W|}{N_i N_j} \sum_{i'=1}^{N_i} \sum_{j'=1}^{N_j} \mathbf{1}[d(i', j'] \leq r] \cdot e(i', j'). \tag{16}$$

For a homogeneous Poisson process, the expected value of $\sum_{j'=1}^{N_j} \mathbf{1}[d(i', j') \leq r]$, the number of type j cells within distance r of type-i cell i', is $N_j \times \pi r^2 / |W|$. Thus, ignoring the edge correction,

$$E\{K_{(i,j)}(r)\} = E\{K_{(i,j)}(i' \mid r)\} = \pi r^2.$$

This baseline represents the expected value of $K_{(i,j)}(r)$, given random spatial organization. The cross-L function applies a variance-stabilizing transformation to the cross-K function:

$$L_{(i,j)}(r) = \sqrt{\frac{K_{(i,j)}(r)}{\pi}} - r \tag{17}$$

The representations of $K_{(i,j)}(r)$ and $L_{(i,j)}(r)$ allow us to resample local contributions (via the Loh bootstrap) while preserving the relationship between within-sample bootstrap estimates and

the observed global statistic.

A.1.2 Edge Correction

Spatial statistics near tissue boundaries are subject to edge effects: cells near the boundary have incomplete neighborhoods (neighborhoods may extend beyond tissue bounds), potentially biasing estimates.

PANORAMIC uses translation edge correction, which assumes spatial stationarity and corrects for edge effects by upweighting point pairs that could have been observed fully elsewhere in the window. For example, if two cells are d units apart, their interaction is only fully observable when both cells are at least d units from the nearest edge. Translation correction accounts for this by adjusting the weight of such pairs.

Alternative edge corrections (e.g., isotropic, border method) are available in the `spatstat` package and can be used by advanced users, but translation correction is the default and provides good performance across tissue geometries.

A.2 Within-Sample Variance Estimation: Loh Spatial Bootstrap

The Loh spatial bootstrap is a non-parametric resampling method designed for spatially dependent data [1, 2]. Unlike standard bootstrap methods that assume independence, the Loh method preserves spatial correlation structure during resampling.

Algorithm:

1. For a given cell type pair (i, j) and sample k, compute local cross-K values $\{K_{(i,j),k}(i' \mid r) | 1 \leq i' \leq N_i\}$.

2. Conduct spatial bootstrap, which is approximately equivalent to resampling these local values with replacement (preserving spatial structure by keeping cells spatially located).

3. Reconstruct the global cross-K estimate from resampled local values:

$$K^{(b)}_{(i,j),k}(r) = N_i^{-1} \sum_{i'=1}^{N_i} w^{(b)}_{i'} K^{*}_{(i,j),k}(i' \mid r)$$

   for bootstrap iteration b, where $w^{(b)}_{i'}$ is the number of times type-i cell i' is selected in the bth bootstrap and $K^{*}_{(i,j),k}(i' \mid r)$ is local K value in the spatial bootstrap, since it could be different from $K_{(i,j),k}(i' \mid r)$ if the $i'$the type i cell is close to the boundary of the "plate" used for spatial bootstrap. In practice, the difference between them is often ignored for fast computation.

4. Obtain the global L statistic $L^{(b)}_{(i,j),k}(r)$ based on $K^{(b)}_{(i,j),k}(r)$.

5. Repeat B times to generate the bootstrap estimates $\{L^{(b)}_{(i,j),k}(r), b = 1, \cdots, B\}$, where B is a reasonably big number such as $B = 100$.

6. Estimate bootstrap variance:

$$\hat{\sigma}^2_{(i,j),k}(r) = \text{var}\left\{L^{(1)}_{(i,j),k}(r), L^{(2)}_{(i,j),k}(r), \ldots, \hat{L}^{(B)}_{(i,j),k}(r)\right\}.$$

This approach differs from parametric bootstrap (which requires fitting a spatial model) and standard non-parametric bootstrap (which would assume independence). The Loh bootstrap is computationally efficient and does not require model specification, making it ideal for exploratory spatial analysis.

A.3 Between-Sample Pooling: Hierarchical Random-Effects Meta-Analysis

For each cell type pair (i, j), we pool colocalization estimates across samples within each group using a two-level hierarchical random-effects model.

Level 1 (Within-Sample Observation Model):

$$L_{(i,j),k}(r) \sim \mathcal{N}\left(l_{(i,j),k}(r), \hat{\sigma}^2_{(i,j),k}(r)\right) \tag{18}$$

The observed colocalization $\hat{L}_{(i,j),k}(r)$ (from sample k) is normally distributed around the true underlying colocalization $l_{(i,j),k}(r)$ with variance $\hat{\sigma}^2_{(i,j),k}(r)$ estimated via spatial bootstrap.

Level 2 (Between-Sample Random Effects Model):

$$l_{(i,j),k}(r) \sim \mathcal{N}(\mu_{(i,j)}(r), \tau^2_{(i,j)}(r)) \tag{19}$$

The true sample-specific colocalization values are normally distributed around a group-level mean $\mu_{(i,j)}$ with between-sample variance $\tau^2_{(i,j)}$.

This two-level hierarchical random effects model is equivalent to the marginal model:

$$L_{(i,j),k}(r) \sim \mathcal{N}\left(\mu_{(i,j)}(r), \hat{\sigma}^2_{(i,j),k}(r) + \tau^2_{(i,j)}(r)\right), \tag{20}$$

where $\mu_{(i,j)}(r)$ is the parameter of the primary interest.

A.3.1 Estimating Heterogeneity: Sidik-Jonkman Estimator

Multiple estimators exist for $\tau^2_{(i,j)}(r)$ (heterogeneity variance), each with different statistical properties. PANORAMIC uses the Sidik-Jonkman (SJ) estimator by default for the following reasons:

Robust Type I error rates [3, 4]: SJ has been shown to maintain appropriate Type I error rates across varying sample sizes ($K = 2$ to 100) and heterogeneity levels, whereas alternatives (REML, DerSimonian-Laird) often produce inflated error rates.

Small-sample performance: SJ performs well when $K < 10$, the typical scenario for spatial omics studies.

Accounts for varying precision: SJ uses each sample's within-sample variance $\hat{\sigma}^2_{(i,j),k}(r)$ to estimate residual variance, appropriately weighting studies with different precision.

The SJ variance estimator is:

$$\hat{\tau}^2_{(i,j)}(r) = \left[\frac{1}{K-1}\sum_{k=1}^{K}\frac{\{L_{(i,j),k}(r) - \tilde{\mu}_{(i,j)}(r)\}^2}{\hat{\sigma}^2_{(i,j),k}(r)} - 1\right] \times \frac{1}{K}\sum_{k=1}^{K}\hat{\sigma}^2_{(i,j),k}(r) \tag{21}$$

where

$$\tilde{\mu}_{(i,j)}(r) = \sum_{k=1}^{K} L_{(i,j),k}(r) \times \frac{\hat{\sigma}^{-2}_{(i,j),k}(r)}{\sum_{k=1}^{K}\hat{\sigma}^{-2}_{(i,j),k}(r)}$$

is a simple inverse-variance weighted estimator of $\mu_{(i,j)}$.

PANORAMIC also supports alternative estimators available in the `metafor` R package (REML, DL, Paule-Mandel, etc.) for users with specific assumptions or preferences.

A.3.2 Pooled Estimates and Standard Errors

Given the SJ variance estimator $\hat{\tau}^2_{(i,j)}(r)$ for $\tau^2_{(i,j)}(r)$, the final estimate for the group mean is a refined inverse variance estimator

$$\hat{\mu}_{(i,j)}(r) = \frac{\sum_{k=1}^{K}\left\{\hat{\sigma}^2_{(i,j),k}(r) + \hat{\tau}^2_{\mathrm{SJ}}(r)\right\}^{-1} \times L^{(i,j),k}(r)}{\sum_{k=1}^{K}\left\{\hat{\sigma}^2_{(i,j),k}(r) + \hat{\tau}^2_{\mathrm{SJ}}(r)\right\}^{-1}}, \tag{22}$$

whose variance can be estimated by

$$\hat{\sigma}^2_{(i,j)} = \left\{\sum_{k=1}^{K}\frac{1}{\hat{\sigma}^2_{(i,j),k}(r) + \hat{\tau}^2_{\mathrm{SJ},(i,j)}(r)}\right\}^{-1}. \tag{23}$$

This variance estimator incorporates both sources of variability, yielding appropriate confidence interval for $\mu_{(i,j)}(r)$.

A.4 Differential Testing and Multiple Correction

For group comparisons (group A vs group B), we perform separate meta-analyses for each group, yielding estimates$\hat{\mu}^{(A)}_{(i,j)}$ and $\hat{\mu}^{(B)}_{(i,j)}$ with corresponding variances. The Wald test statistic for two-

group comparison is:

$$Z_{(i,j)} = \frac{\hat{\mu}^{(A)}_{(i,j)}(r) - \hat{\mu}^{(B)}_{(i,j)}(r)}{\sqrt{\hat{\sigma}^{(A)}_{(i,j)}(r)^2 + \hat{\sigma}^{(B)}_{(i,j)}(r)^2}}. \tag{24}$$

Two-sided p-values are derived from the standard normal distribution. Multiple testing correction is applied across all p cell type pairs using false discovery rate control (Benjamini-Hochberg procedure) with target $\alpha = 0.05$.

Assumption: Independence between pairs. This test assumes independence between different cell type pairs, which is reasonable given that pairs involve distinct cell types. However, pairs sharing a cell type (e.g., A-B and A-C) are correlated; multivariate extensions or correction methods for related outcomes are warranted.

A.5 Network Analysis and Higher-Order Spatial Organization

Network construction from pairwise Z-scores proceeds as follows:

Asymmetry handling: The cross-L function is directional ($L^{(i,j),k}(r) \neq L^{(j,i),k}(r)$), so differential testing yields two Z-scores per unordered pair.

Symmetrization: Form a matrix M with rows and columns representing cell types; fill with Z-scores from pairwise testing. Symmetrize via $M_{\text{sym}} = \frac{1}{2}(M + M^\top)$.

Filtering: Retain edges with FDR < 0.1 and positive weights (CLR-enriched associations), setting negative weights to zero to ensure compatibility with community detection algorithms.

Clustering: Apply Leiden clustering (resolution = 1.25) to identify coherent subnetworks.

Validation: For identified clusters, compute average minimum distances among cluster members, then compare across groups using one-sided t-tests.

B Supplementary Simulation Details

B.1 Spatial point processes

Spatial point process models (SPP) provide a natural framework for generating synthetic spatial omics data with user-specified properties, making them a useful tool for evaluating the performance of PANORAMIC. A SPP is defined over a two-dimensional spatial domain D and parameterized by an intensity function $\lambda_c(x, y) \in \mathbb{R}^+$ for each cell type c, specifying the expected density of cells at location (x, y). Superimposing intensity functions for multiple cell types yields multi-type spatial patterns with controlled colocalization structure.

B.2 Intra-Sample Variance Estimation Study

B.2.1 Spatial Point Process Specifications

Three spatial point process configurations were generated over a 2000×2000 window with five cell types:

Homogeneous Point Process (Complete Spatial Randomness):

All cell types distributed uniformly at random with constant intensity functions:

- $\lambda_{(A)}(x, y) = 2 \times 10^{-4}$ (main type A)
- $\lambda_{(B)}(x, y) = 1.5 \times 10^{-4}$ (main type B)
- $\lambda_{(C)}(x, y) = 1 \times 10^{-4}$ (main type C)
- $\lambda_{(\text{Rare 1})}(x, y) = 1 \times 10^{-5}$ (rare type 1)
- $\lambda_{(\text{Rare 2})}(x, y) = 5 \times 10^{-6}$ (rare type 2)

Expected cell counts: A $\approx$ 400, B $\approx$ 300, C $\approx$ 200, Rare1 $\approx$ 20, Rare2 $\approx$ 10.

Divergent Point Process (Spatial Segregation):

Cell types A and B separated into opposite spatial regions via exponential intensity functions:

- $\eta \sim \text{Uniform}(1 \times 10^{-10}, 5 \times 10^{-3})$
- $\lambda_{(A)}(x, y) = \eta e^{-\eta x}$ (A concentrated at left)
- $\lambda_{(B)}(x, y) = \eta e^{-\eta(2000-x)}$ (B concentrated at right)
- $\lambda_{(C)}(x, y) = 1 \times 10^{-4}$ (C random)
- $\lambda_{(\text{Rare 1})}(x, y) = 1 \times 10^{-5}$, $\lambda_{(\text{Rare 2})}(x, y) = 5 \times 10^{-6}$ (random)

This mimics tumor-stroma compartmentalization.

Clustered Point Process (Cell Recruitment):

Type B cells positioned as offspring around type A parent cells:

1. Sample parent points (type A) from $\lambda_{(A)}(x, y) = 1 \times 10^{-5}$.
2. For each parent A_i, sample number of offspring: $N_{B_i} \sim \text{Poisson}(7) + 1$.
3. For each offspring j, sample position: $B_j \sim \mathcal{N}(A_i, \Sigma)$, where $\Sigma = 175$ (pixel variance).

4. Sample remaining types (C, Rare1, Rare2) uniformly as in homogeneous process.

Ground Truth Variance Calculation:

For each SPP configuration Ω_k:

1. Generate 1000 independent realizations $\omega_{k,1}, \ldots, \omega_{k,1000}$.
2. Compute global cross-L statistic $L_{((i,j),k),l}(r)$ for realization $l = 1, \cdots, 1000$ at $r = 75\ \mu m$.
3. Estimate ground truth variance: $\sigma^2_{(i,j),k}(r) = \mathrm{var}(L_{((i,j),k),1}(r), \ldots, L_{((i,j),k),1000}(r))$.
4. Bootstrap Variance Estimation:

   For each of the 1000 realizations, apply Loh spatial bootstrap (100 iterations) independently and compute bootstrap variance $\hat{\sigma}^2_{(i,j),k,l}(r)$ based on $\omega_{k,l}, l = 1, \cdots, 1000$.
5. Compute the correlation coefficients between bootstrap variance estimates $\hat{\sigma}^2_{(i,j),k}(r)$ with ground truth $\sigma^2_{(i,j),k,l}(r)$ across 25 ordered cell type pairs, $\rho_{k,l}(r) = cor\left(\hat{\sigma}^2_{(i,j),k}(r), \sigma^2_{(i,j),k,l}(r)\right)$ for $l = 1, \cdots, 1000$.

The distribution of $\{\rho_{k,l}, l = 1, \cdots, 1000\}$ reflects the quality of the bootstrap variance estimator across different cell type pairs.

B.3 Inter-Sample Variance Estimation Study

B.3.1 Hierarchical Simulation Framework

A baseline clustered SPP (as described above) serves as the population generative model $\mathbf{\Omega}$. To create K variant models $\Omega_1, \ldots, \Omega_K$ representing samples with common underlying biology but differing spatial realizations, we introduce stochastic perturbations:

Parent Point Intensity (Sample-Specific):

$$\lambda_{(A),k}(x, y) = 1 \times 10^{-5} + U_k, \quad U_k \sim \mathrm{Uniform}(0, 0.0001) \tag{25}$$

Offspring Count (Sample-Specific):

$$N_{B_i,k} \sim \mathrm{Poisson}(\gamma_k) + 1, \quad \gamma_k \sim \mathrm{NegativeBinomial}(\alpha = 10, \beta = 2) + 3 \tag{26}$$

Offspring Dispersion (Sample-Specific):

$$B_{j,k} \sim \mathcal{N}(A_i, \Sigma_k), \quad \Sigma_k = 175 + \epsilon_k, \quad \epsilon_k \sim \mathcal{N}(0, 100) \tag{27}$$

These perturbations create realistic inter-sample heterogeneity: each variant model has different clustering patterns while maintaining shared underlying structure.

Establishing Ground Truth:

For each variant Ω_k,

1. Generate $N = 100$ realizations. For cell type pair (i, j):
2. Compute ground truth sample mean: $l_{(i,j),k}(r) = 100^{-1} \sum_{l=1}^{100} L_l^{(i,j),k}(r)$
3. Compute ground truth group means: $\mu_{(i,j)}(r) = K^{-1} \sum_{k=1}^{K} l_{(i,j),k}(r)$
4. Compute ground truth inter-sample variance: $\tau^2_{(i,j)} = K^{-1} \sum_{k=1}^{K} \left\{ l_{(i,j),k}(r) - \mu_{(i,j)}(r) \right\}^2$

Realistic Data Analysis Scenario (PANORAMIC Input):

- The Proposed Method
  - From each variant Ω_k, use only one realization $\omega_{k,1}$.
  - Conduct spatial bootstrap (100 iterations) to obtain the variance estimator $\hat{\sigma}^2_{(i,j),k}(r)$
  - Conduct the Sidik-Jonkman meta-analysis to obtain $\hat{\mu}_{(i,j)}(r), \hat{\tau}^2_{(i,j)}(r)$, and $\hat{\sigma}^2_{(i,j)}(r)$.
- The Reference Method (Naive Estimator):
  - Treat $L_{(i,j),k}(r)$ as fixed values (ignoring within-sample uncertainty):

$$\hat{\mu}^{\text{naive}}_{(i,j)}(r) = \frac{1}{K} \sum_{k=1}^{K} L_{(i,j),k}(r) \tag{28}$$

$$\hat{\tau}^{2,\text{naive}}_{(i,j)}(r) = \frac{1}{K} \sum_{k=1}^{K} \left\{ L_{(i,j),k}(r) - \hat{\mu}^{\text{naive}}_{(i,j)}(r) \right\}^2. \tag{29}$$

Performance Metrics:

- Compute RMSE for each pair and sample size of $[2, 100]$, 5 cell types, therefore 25 ordered pairs:

$$\text{RMSE}_{\mu} = \sqrt{\frac{1}{25} \sum_{(i,j)} \left\{ \hat{\mu}_{(i,j)}(r) - \mu_{(i,j)}(r) \right\}^2} \tag{30}$$

$$\text{RMSE}_{\tau^2} = \sqrt{\frac{1}{25} \sum_{(i,j)} \left\{ \hat{\tau}^2_{(i,j)}(r) - \tau^2_{(i,j)}(r) \right\}^2} \tag{31}$$

C Supplementary Discussion: Method Comparisons

C.1 Comparison to spicyR

spicyR [5] is a widely used approach for analyzing colocalization across multiple spatial omics samples.

Key differences from PANORAMIC: Within-sample uncertainty not modeled: spicyR treats each tissue core's colocalization estimate as a fixed measurement $L^{(i,j),k}(r)$, ignoring the spatial sampling uncertainty $\sigma^2_{(i,j),k}(r)$, which may vary with k.

Homogeneous variance assumption: spicyR assumes equal variance across samples ($\sigma_1(r)^2$ shared across all cores), whereas PANORAMIC allows sample-specific within-sample variances.

Spatial correlation not preserved: spicyR's random intercept does not preserve spatial correlation structure when estimating uncertainty.

Consequence: When tissue cores have high sampling variability (small numbers of cells, spatial heterogeneity), ignoring $\sigma^2_{(i,j),k}(r)$ results in inefficient estimator for $\mu_{(i,j)}(r)$ and invalid statistical inference.

Application result: In the colorectal cancer dataset, spicyR detected 0 significant associations at FDR < 0.05, whereas PANORAMIC detected 9, all biologically coherent with known CLR organization. This difference in discovery rate demonstrates the practical importance of accounting for within-sample uncertainty.

Table 1. spicyR colocalization results $r = [0, 75]\mu$m on Schürch et al. [6]

from	to	intercept	coefficient	p.value	adj.pvalue
smooth_muscle	tregs	-5727.098	5541.647	0.008	0.504
tregs	smooth_muscle	-5595.164	5345.183	0.010	0.504
plasma_cells	vasculature	3988.180	-4105.771	0.021	0.504
vasculature	granulocytes	2324.541	-3428.167	0.035	0.504
tumor_cells	smooth_muscle	-3399.200	-3109.254	0.037	0.504
tregs	tregs	-494.462	7381.818	0.037	0.504
vasculature	plasma_cells	4058.565	-4103.832	0.039	0.504
b_cells	tumor_cells	-2640.422	-3859.736	0.043	0.504
tumor_cells	b_cells	-2593.483	-3909.010	0.043	0.504
tumor_cells	tumor_cells	10919.252	5714.562	0.046	0.504
tumor_cells	vasculature	-2787.986	-2436.747	0.046	0.504
granulocytes	vasculature	1985.482	-3136.788	0.049	0.504
smooth_muscle	tumor_cells	-3357.175	-3025.888	0.051	0.504
stroma	b_cells	-453.745	2999.322	0.055	0.504
b_cells	stroma	-487.858	3029.825	0.057	0.504
vasculature	tumor_cells	-2995.610	-2235.762	0.059	0.504
granulocytes	cd68_macrophages	267.863	4069.313	0.062	0.504
smooth_muscle	b_cells	-6455.744	3656.440	0.064	0.504

b_cells	smooth_muscle	-6514.209	3546.926	0.066	0.504
cd68_macrophages	b_cells	2395.230	-4788.336	0.102	0.640
cd68_macrophages	granulocytes	566.527	3693.985	0.105	0.640
cd68_macrophages	cd68_macrophages	343.119	6200.648	0.106	0.640
b_cells	cd68_macrophages	2477.877	-4690.662	0.113	0.640
cd8_t_cells	stroma	827.859	1623.525	0.119	0.640
tumor_cells	plasma_cells	-2549.006	-2229.751	0.127	0.640
plasma_cells	tumor_cells	-2595.025	-2192.480	0.131	0.640
granulocytes	smooth_muscle	-1518.652	-2669.749	0.132	0.640
smooth_muscle	granulocytes	-1524.682	-2635.843	0.133	0.640
stroma	cd8_t_cells	955.436	1521.745	0.135	0.640
cd68_cd163_macrophages	plasma_cells	4907.868	-2156.185	0.138	0.640
stroma	cd4_t_cells_cd45ro	499.899	1584.310	0.144	0.640
b_cells	cd68_cd163_macrophages	1850.388	1943.592	0.152	0.640
plasma_cells	cd68_cd163_macrophages	4878.934	-2010.367	0.156	0.640
cd68_macrophages	tumor_cells	-1776.942	2886.425	0.156	0.640
tregs	stroma	40.283	2086.337	0.157	0.640
cd68_cd163_macrophages	b_cells	1874.868	1944.975	0.160	0.640
cd4_t_cells_cd45ro	stroma	638.295	1474.861	0.171	0.659
tumor_cells	cd68_macrophages	-1595.124	2780.441	0.176	0.659
cd4_t_cells_cd45ro	smooth_muscle	-2633.594	2169.743	0.180	0.659
stroma	tregs	44.052	2016.220	0.183	0.659
smooth_muscle	cd4_t_cells_cd45ro	-2599.143	2080.671	0.201	0.664
smooth_muscle	cd8_t_cells	-3442.207	2033.953	0.204	0.664
cd8_t_cells	smooth_muscle	-3625.275	2008.411	0.208	0.664
cd68_cd163_macrophages	tregs	1714.807	1777.626	0.219	0.664
cd4_t_cells_cd45ro	cd4_t_cells_cd45ro	9908.319	-3103.497	0.221	0.664
granulocytes	cd8_t_cells	115.085	1787.988	0.222	0.664
tumor_cells	cd4_t_cells_cd45ro	-3155.158	-1840.997	0.224	0.664
cd8_t_cells	granulocytes	105.394	1713.080	0.229	0.664
granulocytes	cd68_cd163_macrophages	-145.247	1125.877	0.231	0.664
tregs	cd68_cd163_macrophages	1821.268	1692.068	0.231	0.664
cd4_t_cells_cd45ro	tumor_cells	-3091.602	-1796.837	0.241	0.674
plasma_cells	plasma_cells	14272.668	-5049.453	0.243	0.674
granulocytes	tregs	-2133.049	2566.707	0.260	0.694
granulocytes	plasma_cells	924.908	-2003.922	0.260	0.694
cd68_cd163_macrophages	granulocytes	-91.003	1066.132	0.266	0.696
b_cells	b_cells	12756.110	-4789.251	0.272	0.700
smooth_muscle	cd68_cd163_macrophages	-903.530	1324.127	0.290	0.721
stroma	stroma	4081.503	1668.619	0.303	0.721
tregs	granulocytes	-1951.735	2292.233	0.313	0.721
b_cells	tregs	405.335	2538.247	0.314	0.721
smooth_muscle	vasculature	3184.197	-1883.084	0.318	0.721
tregs	b_cells	679.199	2554.134	0.322	0.721
vasculature	cd68_macrophages	-1627.330	-1745.026	0.326	0.721
cd68_macrophages	vasculature	-1669.495	-1709.736	0.328	0.721
cd68_cd163_macrophages	smooth_muscle	-925.584	1201.882	0.335	0.721
plasma_cells	granulocytes	784.259	-1667.756	0.342	0.721
tregs	plasma_cells	-771.674	2907.117	0.342	0.721

plasma_cells	tregs	-783.316	2915.105	0.344	0.721
tumor_cells	cd68_cd163_macrophages	-3158.497	-1162.199	0.345	0.721
cd68_cd163_macrophages	tumor_cells	-3263.787	-1134.382	0.357	0.734
tregs	tumor_cells	-6384.201	2017.313	0.378	0.750
cd8_t_cells	cd68_cd163_macrophages	3426.126	811.010	0.380	0.750
cd68_cd163_macrophages	cd8_t_cells	3445.813	832.912	0.380	0.750
smooth_muscle	smooth_muscle	16878.756	-2941.805	0.387	0.752
b_cells	cd8_t_cells	6908.467	-1904.395	0.394	0.756
tumor_cells	tregs	-6203.785	1905.290	0.399	0.756
tumor_cells	cd8_t_cells	-2968.781	-1061.369	0.411	0.757
granulocytes	b_cells	-3309.885	1494.804	0.417	0.757
vasculature	smooth_muscle	3069.353	-1532.221	0.433	0.757
b_cells	granulocytes	-3196.338	1450.256	0.433	0.757
cd8_t_cells	b_cells	6785.670	-1725.938	0.441	0.757
tumor_cells	granulocytes	1179.857	-1186.808	0.441	0.757
cd8_t_cells	cd8_t_cells	10776.284	-1893.749	0.444	0.757
stroma	cd68_macrophages	2161.006	-1116.175	0.450	0.757
cd8_t_cells	tumor_cells	-3130.270	-981.753	0.452	0.757
cd68_macrophages	stroma	2048.489	-1118.271	0.452	0.757
cd68_cd163_macrophages	cd68_cd163_macrophages	7344.615	-1008.816	0.459	0.759
cd4_t_cells_cd45ro	b_cells	6216.397	1505.842	0.478	0.782
tregs	cd68_macrophages	-2573.229	1823.194	0.489	0.792
granulocytes	tumor_cells	864.228	-990.426	0.522	0.827
cd4_t_cells_cd45ro	plasma_cells	4093.115	-1282.801	0.527	0.827
granulocytes	cd4_t_cells_cd45ro	1163.346	-953.547	0.532	0.827
cd68_macrophages	tregs	-2428.503	1654.616	0.534	0.827
b_cells	cd4_t_cells_cd45ro	6240.684	1210.925	0.561	0.845
plasma_cells	smooth_muscle	-2966.074	1061.061	0.561	0.845
plasma_cells	b_cells	3189.530	-1694.938	0.564	0.845
vasculature	vasculature	14928.286	1468.706	0.589	0.874
smooth_muscle	plasma_cells	-2934.031	920.402	0.613	0.888
b_cells	plasma_cells	3119.637	-1483.882	0.615	0.888
tumor_cells	stroma	-1815.731	-520.357	0.620	0.888
smooth_muscle	stroma	191.108	708.815	0.623	0.888
vasculature	tregs	-1197.850	856.892	0.642	0.906
plasma_cells	stroma	2127.417	659.958	0.652	0.906
plasma_cells	cd4_t_cells_cd45ro	3902.970	-901.308	0.655	0.906
cd4_t_cells_cd45ro	cd68_cd163_macrophages	2371.410	435.965	0.664	0.911
tregs	vasculature	-1098.015	747.880	0.688	0.914
cd4_t_cells_cd45ro	granulocytes	1072.998	-602.409	0.693	0.914
cd68_cd163_macrophages	vasculature	2151.300	-403.094	0.696	0.914
plasma_cells	cd8_t_cells	3013.626	-710.707	0.709	0.914
smooth_muscle	cd68_macrophages	-3115.918	769.017	0.711	0.914
stroma	smooth_muscle	264.864	519.125	0.715	0.914
vasculature	cd8_t_cells	1116.967	-503.140	0.716	0.914
cd68_macrophages	cd4_t_cells_cd45ro	-124.485	-583.731	0.717	0.914
cd8_t_cells	vasculature	1003.296	-482.193	0.727	0.918
cd68_macrophages	smooth_muscle	-3191.763	683.476	0.740	0.922
stroma	tumor_cells	-1961.584	-353.031	0.743	0.922

cd8_t_cells	plasma_cells	2861.746	-596.089	0.759	0.926
cd8_t_cells	cd4_t_cells_cd45ro	6153.362	-525.427	0.767	0.926
cd4_t_cells_cd45ro	vasculature	2088.931	-373.343	0.784	0.926
cd4_t_cells_cd45ro	cd68_macrophages	-62.753	-433.751	0.790	0.926
cd8_t_cells	tregs	4358.871	601.779	0.791	0.926
cd68_macrophages	cd68_cd163_macrophages	2659.149	260.256	0.796	0.926
vasculature	cd4_t_cells_cd45ro	1967.803	-349.407	0.797	0.926
cd68_cd163_macrophages	cd4_t_cells_cd45ro	2413.094	251.010	0.802	0.926
cd68_cd163_macrophages	stroma	1740.278	228.914	0.808	0.926
cd4_t_cells_cd45ro	cd8_t_cells	6364.279	-442.826	0.810	0.926
cd68_macrophages	plasma_cells	-2166.402	-427.931	0.834	0.935
vasculature	stroma	2429.371	294.537	0.840	0.935
stroma	plasma_cells	2364.976	305.044	0.841	0.935
granulocytes	stroma	146.192	270.201	0.847	0.935
tregs	cd8_t_cells	4645.330	423.525	0.854	0.935
stroma	vasculature	2380.357	263.640	0.857	0.935
vasculature	b_cells	-1676.136	287.956	0.870	0.942
cd8_t_cells	cd68_macrophages	2628.548	-255.691	0.877	0.943
cd68_cd163_macrophages	cd68_macrophages	2794.833	145.850	0.885	0.944
stroma	cd68_cd163_macrophages	1870.026	123.149	0.894	0.944
plasma_cells	cd68_macrophages	-2104.216	-246.998	0.905	0.944
vasculature	cd68_cd163_macrophages	2060.363	-122.854	0.905	0.944
granulocytes	granulocytes	13770.900	-209.211	0.946	0.978
tregs	cd4_t_cells_cd45ro	4051.913	-96.412	0.958	0.978
cd68_macrophages	cd8_t_cells	2461.965	-85.718	0.958	0.978
stroma	granulocytes	352.763	44.382	0.973	0.985
b_cells	vasculature	-1476.860	-45.128	0.980	0.985
cd4_t_cells_cd45ro	tregs	4083.853	-33.941	0.985	0.985

D Supplementary Table

Table 2. PANORAMIC colocalization results $r = 75\mu$m on Schürch et al. [6].

ct1	ct2	p_diff	fdr_diff
(b_cells)	(b_cells)	0.000	0.002
(cd4_t_cells_cd45ro)	(tregs)	0.000	0.004
(cd4_t_cells_cd45ro)	(cd4_t_cells_cd45ro)	0.001	0.028
(cd4_t_cells_cd45ro)	(b_cells)	0.001	0.035
(cd8_t_cells)	(b_cells)	0.002	0.035
(b_cells)	(cd4_t_cells_cd45ro)	0.002	0.035
(b_cells)	(cd8_t_cells)	0.002	0.035
(cd4_t_cells_cd45ro)	(cd8_t_cells)	0.001	0.035
(cd8_t_cells)	(cd4_t_cells_cd45ro)	0.002	0.040
(cd8_t_cells)	(cd8_t_cells)	0.006	0.083
(cd8_t_cells)	(tregs)	0.015	0.196
(tregs)	(tregs)	0.021	0.256
(tregs)	(cd4_t_cells_cd45ro)	0.041	0.433
(smooth_muscle)	(smooth_muscle)	0.042	0.433

(cd68_cd163_macrophages)	(cd68_cd163_macrophages)	0.065	0.620
(smooth_muscle)	(stroma)	0.072	0.650
(vasculature)	(cd4_t_cells_cd45ro)	0.114	0.653
(cd68_cd163_macrophages)	(cd68_macrophages)	0.115	0.653
(vasculature)	(cd68_macrophages)	0.118	0.653
(tregs)	(cd8_t_cells)	0.102	0.653
(vasculature)	(cd8_t_cells)	0.109	0.653
(stroma)	(smooth_muscle)	0.093	0.653
(tumor_cells)	(tregs)	0.095	0.653
(vasculature)	(tregs)	0.098	0.653
(cd8_t_cells)	(vasculature)	0.116	0.653
(smooth_muscle)	(vasculature)	0.098	0.653
(cd4_t_cells_cd45ro)	(cd68_macrophages)	0.146	0.703
(vasculature)	(smooth_muscle)	0.145	0.703
(plasma_cells)	(tregs)	0.146	0.703
(tregs)	(tumor_cells)	0.145	0.703
(vasculature)	(b_cells)	0.152	0.704
(tregs)	(b_cells)	0.171	0.771
(cd4_t_cells_cd45ro)	(vasculature)	0.190	0.828
(smooth_muscle)	(cd68_macrophages)	0.205	0.852
(b_cells)	(tumor_cells)	0.207	0.852
(tumor_cells)	(cd68_macrophages)	0.232	0.909
(b_cells)	(vasculature)	0.234	0.909
(cd8_t_cells)	(cd68_macrophages)	0.305	0.994
(tregs)	(plasma_cells)	0.271	0.994
(granulocytes)	(smooth_muscle)	0.283	0.994
(tumor_cells)	(stroma)	0.311	0.994
(b_cells)	(tregs)	0.304	0.994
(tumor_cells)	(tumor_cells)	0.288	0.994
(tregs)	(vasculature)	0.306	0.994
(vasculature)	(vasculature)	0.284	0.994
(cd68_cd163_macrophages)	(b_cells)	0.576	0.995
(cd68_macrophages)	(b_cells)	0.740	0.995
(granulocytes)	(b_cells)	0.761	0.995
(plasma_cells)	(b_cells)	0.580	0.995
(smooth_muscle)	(b_cells)	0.882	0.995
(stroma)	(b_cells)	0.605	0.995
(tumor_cells)	(b_cells)	0.391	0.995
(cd68_macrophages)	(cd4_t_cells_cd45ro)	0.399	0.995
(granulocytes)	(cd4_t_cells_cd45ro)	0.843	0.995
(plasma_cells)	(cd4_t_cells_cd45ro)	0.601	0.995
(smooth_muscle)	(cd4_t_cells_cd45ro)	0.816	0.995
(stroma)	(cd4_t_cells_cd45ro)	0.718	0.995
(tumor_cells)	(cd4_t_cells_cd45ro)	0.878	0.995
(b_cells)	(cd68_cd163_macrophages)	0.975	0.995
(cd4_t_cells_cd45ro)	(cd68_cd163_macrophages)	0.946	0.995
(cd68_macrophages)	(cd68_cd163_macrophages)	0.463	0.995
(cd8_t_cells)	(cd68_cd163_macrophages)	0.471	0.995
(granulocytes)	(cd68_cd163_macrophages)	0.926	0.995

(plasma_cells)	(cd68_cd163_macrophages)	0.693	0.995
(smooth_muscle)	(cd68_cd163_macrophages)	0.668	0.995
(stroma)	(cd68_cd163_macrophages)	0.693	0.995
(tregs)	(cd68_cd163_macrophages)	0.769	0.995
(tumor_cells)	(cd68_cd163_macrophages)	0.462	0.995
(vasculature)	(cd68_cd163_macrophages)	0.449	0.995
(b_cells)	(cd68_macrophages)	0.403	0.995
(cd68_macrophages)	(cd68_macrophages)	0.904	0.995
(granulocytes)	(cd68_macrophages)	0.706	0.995
(plasma_cells)	(cd68_macrophages)	0.765	0.995
(stroma)	(cd68_macrophages)	0.649	0.995
(tregs)	(cd68_macrophages)	0.517	0.995
(cd68_cd163_macrophages)	(cd8_t_cells)	0.426	0.995
(cd68_macrophages)	(cd8_t_cells)	0.670	0.995
(plasma_cells)	(cd8_t_cells)	0.863	0.995
(smooth_muscle)	(cd8_t_cells)	0.830	0.995
(stroma)	(cd8_t_cells)	0.907	0.995
(tumor_cells)	(cd8_t_cells)	0.754	0.995
(b_cells)	(granulocytes)	0.705	0.995
(cd4_t_cells_cd45ro)	(granulocytes)	0.409	0.995
(cd68_cd163_macrophages)	(granulocytes)	0.618	0.995
(cd68_macrophages)	(granulocytes)	0.343	0.995
(cd8_t_cells)	(granulocytes)	0.337	0.995
(granulocytes)	(granulocytes)	0.721	0.995
(plasma_cells)	(granulocytes)	0.918	0.995
(smooth_muscle)	(granulocytes)	0.392	0.995
(stroma)	(granulocytes)	0.672	0.995
(tregs)	(granulocytes)	0.536	0.995
(tumor_cells)	(granulocytes)	0.435	0.995
(vasculature)	(granulocytes)	0.584	0.995
(b_cells)	(plasma_cells)	0.849	0.995
(cd4_t_cells_cd45ro)	(plasma_cells)	0.537	0.995
(cd68_cd163_macrophages)	(plasma_cells)	0.527	0.995
(cd68_macrophages)	(plasma_cells)	0.700	0.995
(cd8_t_cells)	(plasma_cells)	0.840	0.995
(granulocytes)	(plasma_cells)	0.966	0.995
(plasma_cells)	(plasma_cells)	0.801	0.995
(smooth_muscle)	(plasma_cells)	0.607	0.995
(stroma)	(plasma_cells)	0.675	0.995
(tumor_cells)	(plasma_cells)	0.833	0.995
(vasculature)	(plasma_cells)	0.966	0.995
(b_cells)	(smooth_muscle)	0.884	0.995
(cd4_t_cells_cd45ro)	(smooth_muscle)	0.641	0.995
(cd68_cd163_macrophages)	(smooth_muscle)	0.691	0.995
(cd68_macrophages)	(smooth_muscle)	0.391	0.995
(cd8_t_cells)	(smooth_muscle)	0.830	0.995
(plasma_cells)	(smooth_muscle)	0.610	0.995
(tregs)	(smooth_muscle)	0.817	0.995
(tumor_cells)	(smooth_muscle)	0.773	0.995

(b_cells)	(stroma)	0.502	0.995
(cd4_t_cells_cd45ro)	(stroma)	0.936	0.995
(cd68_cd163_macrophages)	(stroma)	0.517	0.995
(cd68_macrophages)	(stroma)	0.815	0.995
(cd8_t_cells)	(stroma)	0.923	0.995
(granulocytes)	(stroma)	0.934	0.995
(plasma_cells)	(stroma)	0.632	0.995
(stroma)	(stroma)	0.945	0.995
(tregs)	(stroma)	0.687	0.995
(vasculature)	(stroma)	0.805	0.995
(cd68_macrophages)	(tregs)	0.629	0.995
(granulocytes)	(tregs)	0.422	0.995
(smooth_muscle)	(tregs)	0.786	0.995
(stroma)	(tregs)	0.703	0.995
(cd4_t_cells_cd45ro)	(tumor_cells)	0.806	0.995
(cd68_cd163_macrophages)	(tumor_cells)	0.517	0.995
(cd68_macrophages)	(tumor_cells)	0.459	0.995
(cd8_t_cells)	(tumor_cells)	0.487	0.995
(granulocytes)	(tumor_cells)	0.360	0.995
(plasma_cells)	(tumor_cells)	0.735	0.995
(smooth_muscle)	(tumor_cells)	0.970	0.995
(stroma)	(tumor_cells)	0.393	0.995
(vasculature)	(tumor_cells)	0.347	0.995
(cd68_cd163_macrophages)	(vasculature)	0.901	0.995
(cd68_macrophages)	(vasculature)	0.345	0.995
(granulocytes)	(vasculature)	0.915	0.995
(plasma_cells)	(vasculature)	0.974	0.995
(stroma)	(vasculature)	0.841	0.995
(tumor_cells)	(vasculature)	0.427	0.995
(cd68_cd163_macrophages)	(tregs)	0.984	0.997
(cd68_cd163_macrophages)	(cd4_t_cells_cd45ro)	1.000	1.000
(granulocytes)	(cd8_t_cells)	0.995	1.000

E Supplementary Figures

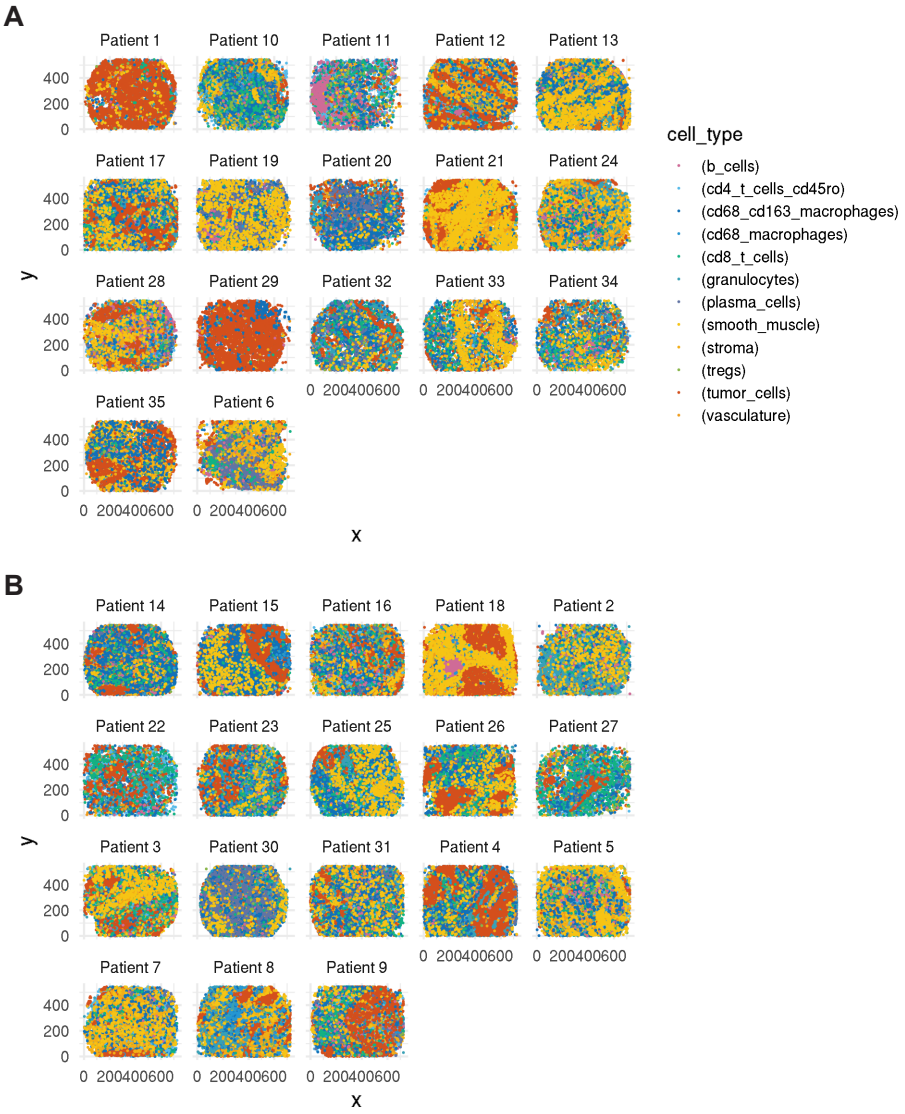

Figure E.1. Spatial overview of all 35 colorectal cancer tissue microarray cores stratified by immune phenotype. **(A)** 17 Crohn's-like reaction (CLR) cores. **(B)** 18 diffuse immune infiltration (DII) cores. 11 cell types are considered in the analysis: B cells, activated CD4+ T cells, CD8+ T cells, granulocytes, plasma cells, smooth muscle cells, stromal cells, regulatory T cells, tumor cells and vasculature cells. Cell typing performed by Schürch et al. [6].

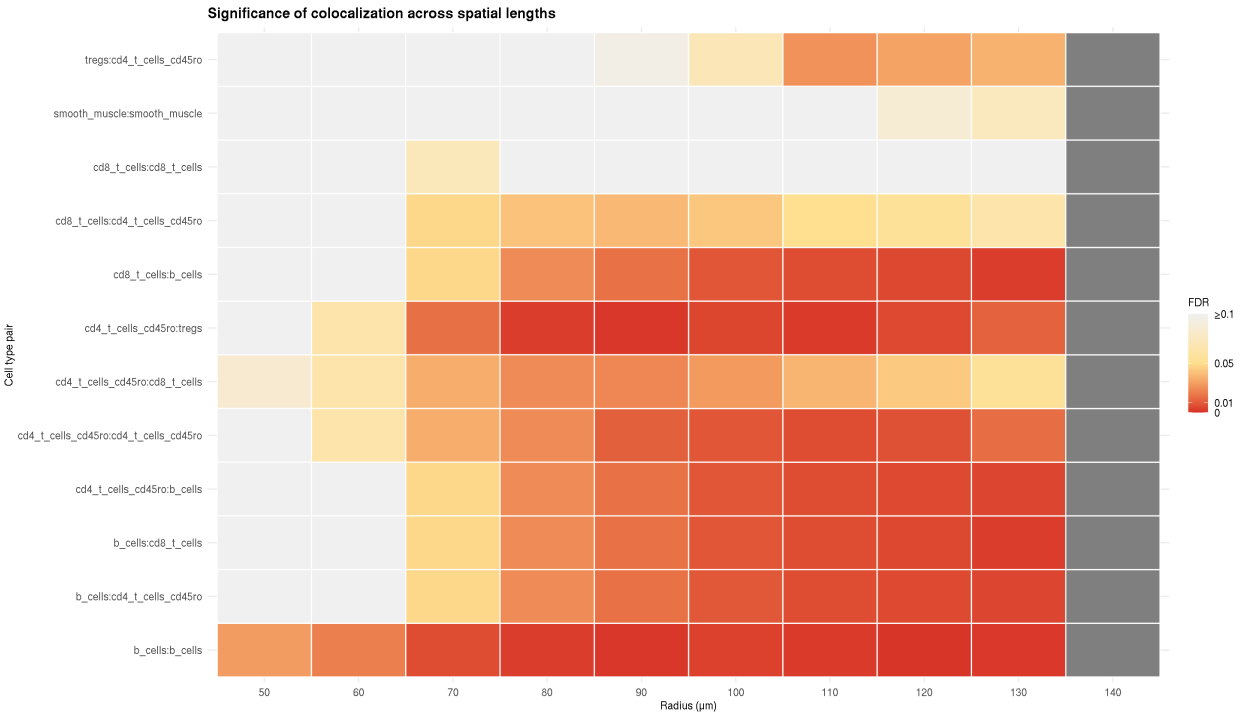

Figure E.2. Consistency of significantly colocalized cell type pairs across multiple radii. Heatmap of FDR-adjusted p-values for CLR vs. DII colocalization testing across cell type pairs (rows) and spatial radii (columns, 50–140 m). Darker colors indicate stronger statistical significance. Light gray indicates adjusted p-values > 0.1. Dark gray indicates that radii extended out of range.

References

1. Loh JM. A Valid and Fast Spatial Bootstrap for Correlation Functions. The Astrophysical Journal 2008 Jul; 681:726–34. DOI: 10.1086/588631
2. Loh JM. Bootstrapping an inhomogeneous point process. Journal of Statistical Planning and Inference 2010 Mar; 140:734–49. DOI: 10.1016/j.jspi.2009.09.003
3. IntHout J, Ioannidis JP, and Borm GF. The Hartung-Knapp-Sidik-Jonkman method for random effects meta-analysis is straightforward and considerably outperforms the standard DerSimonian-Laird method. BMC Medical Research Methodology 2014 Dec; 14:25. DOI: 10.1186/1471-2288-14-25
4. Sidik K and Jonkman JN. Simple Heterogeneity Variance Estimation for Meta-Analysis. Journal of the Royal Statistical Society Series C: Applied Statistics 2005 Apr; 54:367–84. DOI: 10.1111/j.1467-9876.2005.00489.x
5. Canete NP, Iyengar SS, Ormerod JT, Baharlou H, Harman AN, and Patrick E. spicyR: spatial analysis ofin situcytometry data in R. Bioinformatics 2022 May; 38. Ed. by Kelso J:3099–105. DOI: 10.1093/bioinformatics/btac268
6. Schürch CM, Bhate SS, Barlow GL, Phillips DJ, Noti L, Zlobec I, Chu P, Black S, Demeter J, McIlwain DR, Kinoshita S, Samusik N, Goltsev Y, and Nolan GP. Coordinated Cellular Neighborhoods Orchestrate Antitumoral Immunity at the Colorectal Cancer Invasive Front. Cell 2020 Sep; 182:1341–1359.e19. DOI: 10.1016/j.cell.2020.07.005